

A three dimensional extinction map of the Galactic Anticentre from multi-band photometry

B.-Q. Chen,^{1*†} X.-W. Liu,^{1,2*} H.-B. Yuan,^{2†} H.-H. Zhang,¹ M. Schultheis,³
B.-W. Jiang,⁴ Y. Huang,¹ M.-S. Xiang,¹ H.-B. Zhao,⁵ J.-S. Yao,⁵ and H. Lu⁵

¹*Department of Astronomy, Peking University, Beijing 100871, P. R. China*

²*Kavli Institute for Astronomy and Astrophysics, Peking University, Beijing 100871, P. R. China*

³*Universite de Nice Sophia-Antipolis, CNRS, Observatoire de Cote d'Azur, Laboratoire Cassiopee, 06304 Nice Cedex 4, France*

⁴*Department of Astronomy, Beijing Normal University, Beijing 100875, P. R. China*

⁵*Purple Mountain Observatory, Chinese Academy of Sciences, Nanjing 21008, Nanjing, P. R. China*

Accepted ???. Received ???; in original form ???

ABSTRACT

We present a three dimensional extinction map in r band. The map has a spatial angular resolution, depending on latitude, between 3 – 9 arcmin and covers the entire XSTPS-GAC survey area of over 6,000 deg² for Galactic longitude $140 \leq l \leq 220$ deg and latitude $-40 \leq b \leq 40$ deg. By cross-matching the photometric catalog of the Xuyi Schmidt Telescope Photometric Survey of the Galactic Anticentre (XSTPS-GAC) with those of 2MASS and WISE, we have built a multi-band photometric stellar sample of about 30 million stars and applied spectral energy distribution (SED) fitting to the sample. By combining photometric data from the optical to the near-infrared, we are able to break the degeneracy between the intrinsic stellar colours and the amounts of extinction by dust grains for stars with high photometric accuracy, and trace the extinction as a function of distance for low Galactic latitude and thus highly extinguished regions. This has allowed us to derive the best-fit extinction and distance information of more than 13 million stars, which are used to construct the three dimensional extinction map. We have also applied a Rayleigh-Jeans colour excess (RJCE) method to the data using the 2MASS and WISE colour ($H - W2$). The resulting RJCE extinction map is consistent with the integrated two dimensional map deduced using the best-fit SED algorithm. However for individual stars, the amounts of extinction yielded by the RJCE method suffer from larger errors than those given by the best-fit SED algorithm.

Key words: Galaxy: disc, structure, stellar content – ISM: dust, extinction

1 INTRODUCTION

The Milky Way, our own Galaxy, is an archetypical disk galaxy and the only grand-design (barred) spiral for which the individual constituent stars can be spatially resolved and studied multi-dimensionally (in not only three dimensional position and velocity, and in chemical composition, but also in age, size and surface gravity). A major objective of the current astrophysical study is to understand how galaxies assemble and acquire their characteristic structure and properties. Modern large scale surveys, represented by the extremely successful Sloan Digital Sky Survey (SDSS; York et al. 2000), have revolutionized our understanding of galaxy formation and evolution, including the still on-going assemblage process of the Milky Way. The on-going LAMOST Spec-

troscopic Survey of the Galactic Anticentre (LSS-GAC; Liu et al. 2014), a major component of the Galactic surveys with LAMOST (also known as the Guoshoujing Telescope), offers a unique opportunity to reveal the true multi-dimensional structure of the Milky Way and address fundamental questions with regard to the formation and evolution of the Galactic disk, and of the Galaxy as a whole.

Based on the SDSS photometric data, a series of work have attempted to study in detail the distribution of tens of millions of Galactic stars in multi-dimensional space (e.g. Jurić et al. 2008; Ivezić et al. 2008; Bond et al. 2010; Berry et al. 2012). Most of those studies concentrate on regions of high Galactic latitudes ($|b| > 30^\circ$). Although the Sloan Extension for Galactic Understanding and Exploration (SEGUE; Yanny et al. 2009) has reached the low latitude disk, it covers only a few stripes crossing the Galactic plane. In order to provide an input catalog for the LSS-GAC, a multi-band CCD photometric survey of the Galactic Anticentre

* E-mail: bchen@pku.edu.cn (BQC); x.liu@pku.edu.cn (XWL).

† LAMOST Fellow.

tre with the Xuyi 1.04/1.20m Schmidt Telescope (XSTPS-GAC; Zhang et al. 2013, 2014; Liu et al. 2014) has been carried out. The XSTPS-GAC photometric catalog contains more than 100 million stars in the direction of Galactic anticentre (GAC), thus providing an excellent data set to study the Galactic disk, in particular the structures and substructures of the outer disk (truncation, warps and flares), and the Monoceros Ring and other stellar (sub)structures in the GAC direction. The study is however challenged by the presence of a significant amount of prevailing dust extinction that varies on small scales in the GAC direction.

Interstellar extinction is a serious obstacle for the interpretation of stellar populations in the Galaxy, especially for the low latitude regions, specially the Galactic disk. It shows an inhomogeneous clumpy distribution and increases towards the Galactic plane (Burstein & Heiles 1982; Chen et al. 1998; Schultheis et al. 1999; Gonzalez et al. 2012; Nidever et al. 2012). The currently available extinction maps of the GAC regions have various spatial resolutions and coverages. The most commonly used is the whole sky map of Schlegel et al. (1998, SFD hereafter). The SFD map is based on the distribution of dust temperatures derived from the Infrared Astronomical Satellite (IRAS; Neugebauer et al. 1984) and the Diffuse Infrared Background Experiment (DIRBE; Boggess et al. 1992) experiments. The colour temperatures are then calibrated to values of colour excess $E(B - V)$ of dust reddening using colours of background galaxies. Unfortunately, the map suffers from large uncertainties in regions towards the Milky Way disk. Specifically, as stated in the appendix C of SFD, the dust colour temperatures at low Galactic latitudes ($|b| < 5^\circ$) are not well defined and contaminating sources have not been fully removed. Furthermore, as pointed out by Berry et al. (2012), most disk stars are embedded in the dust layer, rather than behind it. As a consequence, the SFD map overestimates the extinction, making it unreliable for most disk stars. Most recently, the *Planck* team publish an all-sky model of the thermal dust emission (Planck Collaboration et al. 2013a), while the Wide-Field Infrared Survey Explorer (WISE) collaboration publishes a full-sky atlas of the Galactic 12- μm dust emission (Meisner & Finkbeiner 2014).

Based on the wide-angle photometric sky surveys in the near-infrared (IR), e.g. the Two Micron All Sky Survey (2MASS, Skrutskie et al. 1997), a number of studies have been carried out to trace the extinction using the near-IR colour excess method (Lombardi & Alves 2001; Lombardi et al. 2011; Majewski et al. 2011; Rowles & Froebrich 2009). Froebrich et al. (2007) present an integrated extinction map of $127 \times 63 \text{ deg}^2$ in the direction of the GAC, with a resolution of 4 arcmin, based on the 2MASS ($J - H$) and ($H - K_s$) colours. Other extinction maps are available for patchy areas of the GAC, such as that obtained using special tracers from the SDSS photometry (e.g. Schlafly et al. 2010; Peek & Graves 2010) or spectroscopic data (e.g. Schlafly & Finkbeiner 2011; Jones et al. 2011). However, for the purpose of detailed studies of the GAC area, a high resolution and homogeneous extinction map covering the whole area of interest is highly desired.

All the extinction maps described above are restricted to two dimensions and refer to integrated extinction along the line of sight. As pointed out above, disk stars are embedded in the dust layer. Thus even for stars in the same direction, the amounts of extinction they suffer from could be quite different due to their different distance information. Several approaches are available to obtain information of distance and derive an extinction map in three dimensions (3D). These include theoretical dust modeling (Chen et al. 1998; Drimmel et al. 2003), comparison of near-IR data of gi-

ants with stellar population synthesis models (Marshall et al. 2006; Chen et al. 2013; Schultheis et al. 2014), ‘‘pair method’’ based on spectroscopic data (Yuan et al. 2014), and tracing stars of special characteristics. Neckel et al. (1980) obtain extinction values and distances using UB V , MK and β photometric data for more than 11,000 O to F stars. Sale et al. (2009) and Sale (2012) propose a technique to obtain 3D extinction maps based on hierarchical Bayesian models. Bailer-Jones (2011), Hanson & Bailer-Jones (2014) and Green et al. (2014) introduce a similar Bayesian approach for estimating the intrinsic stellar parameters and line-of-sight extinction values. For a sample of 73 million stars with the SDSS photometry and a sub-sample of 23 million stars also with complementary 2MASS photometry, Berry et al. (2012) estimate distances and values of extinction of individual stars by fitting the observed optical (and IR) spectral energy distribution (SED). Most recently, Lallement et al. (2014) assemble a data set of colour excess with associated parallax or photometric distances for a sample of 23,000 nearby stars and construct a 3D extinction map of local dust within 2.5 kpc. In the work of Berry et al. (2012), values of extinction up to $A_r \lesssim 2-3$ ($A_r = 0.88A_V$, assuming the extinction law of Cardelli et al. (1989) for a total-to-selective extinction ratio $R_V \equiv A_V/E(B - V) = A_V/(A_B - A_V) = 3.1$) are traced out to a distance of about 2 kpc. When using only the optical SDSS data, distances up to a factor of two can be reached using blue main-sequence stars. For red stars, the distance limit is much smaller. Using only the 2MASS data, Froebrich et al. (2007) trace A_V up to about 10 mag for the GAC region. For the Galactic centre and other high extinction regions, values of A_V can go up to at least 20 mag. (Lombardi & Alves 2001; Nidever et al. 2012). Studies based on the optical data such as the SDSS are limited to A_V of $\lesssim 10$ mag (Schlafly et al. 2010; Peek & Graves 2010).

In this paper, we estimate values of extinction and distance for stars in the XSTPS-GAC photometric catalog. We apply a method similar to that proposed by Berry et al. (2012) to a sample of 30 million stars with complementary IR photometry from the 2MASS and WISE. We also estimate extinction using the RJCE method (Majewski et al. 2011) based on the 2MASS and WISE ($H - W2$) colour. Together with the photometric distances deduced from the dereddened XSTPS-GAC optical photometry (Ivezić et al. 2007; Jurić et al. 2008), we have obtained a 3D extinction map of the GAC region with a spatial resolution, depending on latitude, that varies between 3 – 9 arcmin.

The paper is structured as following: In Section 2 we present the relevant XSTPS-GAC, 2MASS and WISE data. Section 3 describes in detail the method used to derive values of extinction and distance. The results are tested using Monte-Carlo simulations as well as Galaxy models. In Section 4, we present our main results which are discussed in Section 5. We summarize in Section 6.

2 DATA

We first describe the data used in the current work. Bailer-Jones (2011) shows that there is a significant degeneracy between the effective temperature (or intrinsic colours) and extinction derived using just four colours from the artificially *BVJHK* data for artificially reddened *Hipparcos* stars. Berry et al. (2012) show that the degeneracy can be broken when the ($i - z$) colour is also available together with ($g - r$) and ($r - i$), assuming a certain extinction law. However when only the optical g , r and i bands are available, such as in the case of XSTPS-GAC, the degeneracy can not be broken. To overcome the problem, we introduce a sub-sample of the

XSTPS-GAC with matching IR photometry from the 2MASS and WISE to break the degeneracy. We start by briefly describing the XSTPS-GAC, 2MASS and WISE surveys.

2.1 The XSTPS-GAC survey

The Xuyi Schmidt Telescope Photometric Survey of the Galactic Anticentre (XSTPS-GAC), which started collecting data in October 2009 and completed in March 2011, was carried out in order to provide input targets for the LSS-GAC (Liu et al. 2014). The survey collected in the SDSS g , r and i bands using the Xuyi 1.04/1.20 m Schmidt Telescope located on a small hill about 35 km from Xuyi town, north of Nanjing, in the middle-eastern area of China with an elevation of about 180 m above the sea level. The XSTPS-GAC has two components, the main of 5,400 deg² centered on the GAC covering $3\text{ h} \leq \text{R.A.} \leq 9\text{ h}$, and $-10^\circ \leq \text{Dec.} \leq +60^\circ$, and an extension of about 900 deg² covering the M 31/M 33 area. The total survey area is close to 7,000 deg² including the bridging fields connecting the two components. In total, the XSTPS-GAC archives approximately 100 million stars down to a limiting magnitude of about 19 in the r band ($\sim 10\sigma$) with an astrometric accuracy about 0.1" and a global photometric accuracy of about 2% (Liu et al. 2014). The optical broadband atmospheric extinction coefficients and the night sky brightness of the Xuyi Observational Station of the Purple Mountain Observatory are presented by Zhang et al. (2013). A detailed description of the astrometric calibration of the XSTPS-GAC data is given in Zhang et al. (2014). In the current work only data covering the GAC and from the bridging fields, totaling about 6,000 deg², are used. A full account of the observation and data processing will be presented in a future contribution.

The observations were carried out with a thinned 1,096 × 4,096 CCD camera. The effective field-of-view (FoV) of the camera is $1.94^\circ \times 1.94^\circ$ with a sampling of 1.705" per pixel projected on the sky. The integration time was 90 s. The readout time was 43 s using the slow dual channel readout mode. The adjacent fields stepped by 0.95° in RA (i.e. yielding 50% overlap) and 1.90° in Dec. Typically two adjacent stripes along the RA were scanned field by field alternatively. With this observing strategy, the hour angle and zenith distance of the telescope were nearly constant as the observation processed, yielding maximum uniformity. To facilitate the ubercal (global flux calibration), a number of "Z-stripes" were added. The "Z-stripe" fields straddled between two "normal" stripes (i.e. stripes along the RA), to help tie the latter together on a common flux scale. All observations were carried out under dark/grey lunar conditions, with air masses lower than 1.3, except for fields of very low declinations.

A preliminary astrometric calibration was first carried out with the Guide Star Catalog 2.0 (GSC 2.0; Morrison et al. 2001) as the reference using an eight-parameter linear model, yielding an accuracy of about 0.5". The plate distortion was then modeled with a 30-parameters two-dimensional function using the PPMXL as the reference catalog, reaching an accuracy of about 140 mas for individual frames. By combining all frames, we expect to achieve a final astrometric accuracy of about 60 mas. The frames were flat-fielded using super sky flats generated from target frames by clipping all individual stars. Aperture and Point Spread Function (PSF) photometry were carried with a DAOPHOT-based pipeline. A ubercal flux calibration against the SDSS photometry using overlapping fields a photometric accuracy of better than 2% for a single frame and about 2 – 3% for the whole survey sky area. The catalog generated by XSTPS-GAC have been used to select targets during the LAMOST commissioning phase as well as for the Pilot and the

on-going Regular Survey of LSS-GAC. The data will also be used in the reduction and follow-up analyses of the LAMOST data. In addition, taking advantage of its coverage, depth and photometric accuracy, the data will be an asset to study the disk structures (e.g., scale heights and lengths of the thin and thick disks; disk flares, warps and truncation) and constrain the sub-structures (e.g., the Monoceros Ring) in the GAC direction.

In the bottom three panels of Fig. 1 we plot the photometric error and magnitude relation for r band for three different lines of sight ($l = 180^\circ$, $b = 0, -10, 20^\circ$) as examples. Black dots represent XSTPS-GAC measurements. Typically as r band magnitude reaches 18.5, the photometric errors rise to 0.05 mag (see the black lines in the three panels). The black lines in the upper three panels of Fig. 1 plot the normalized star counts as a function of r magnitude, for the XSTPS-GAC data. The distributions show the survey is complete down to a limiting magnitude fainter than 19 mag in r -band. For sources of $r < 16.5$ mag, the measurement errors become smaller than 0.02 mag, which is the estimated systematic error of the global flux calibration of XSTPS-GAC. To account for the calibration uncertainties, all errors are reset to 0.02 mag when the reported errors are smaller than 0.02.

2.2 The 2MASS Survey

The Two Micron All Sky Survey (2MASS) surveyed the entire sky using two 1.3-m aperture telescopes at Mt. Hopkins and CTIO, Chile (Skrutskie et al. 1997). Each 2MASS camera contained three NICMOS3 256×256 HgCdTe detectors, collecting images in three near-IR bands simultaneously: J , H and K_s bands centered at 1.25, 1.65 and $2.16\ \mu\text{m}$, respectively. For point-sources, a signal to noise ratio $S/N = 10$ limit corresponds to a limiting magnitude at $J = 15.8$, $H = 15.1$, and $K_s = 14.3$ mag for virtually the entire sky. Sources brighter than the above limiting magnitudes in the 2MASS Point Source Catalog are believed to be highly complete (>0.99) and reliable (>0.9995). The photometric systematic uncertainties of 2MASS are estimated to be smaller than 0.03 mag, and astrometric uncertainty for these sources is less than 0.2".

2.3 The WISE survey

The Wide-field Infrared Survey Explorer (WISE) surveys the entire sky with a 40 cm telescope on board the satellite (Wright et al. 2010). WISE maps the whole sky in four infrared bands W_1 , W_2 , W_3 and W_4 centered at 3.4, 4.6, 12 and $22\ \mu\text{m}$ respectively, with corresponding spatial angular resolution of 6.1, 6.4, 6.5, and $12.0''$ in the four bands. The WISE All-Sky Data Release area is comprised of 18,240 Atlas Tiles, with each Tile spanning $1.564^\circ \times 1.564^\circ$ in 4095×4095 pixels at a resolution of 1.375" per pixel. The WISE Source Catalog contains positions and photometry for about 564 million point-like and resolved objects. All sources cataloged have a measured S/N greater than 5 in at least one of the four bands. The positions are calibrated against the 2MASS, achieving an accuracy of ~ 200 mas on each axis with respect to the 2MASS reference frame for sources with S/N better than 40. The 5σ photometric sensitivities are 0.068, 0.098, 0.86 and 5.4 mJy (equivalent to Vega magnitudes 16.6, 15.6, 11.3 and 8.0, respectively) at 3.4, 4.6, 12 and $22\ \mu\text{m}$, respectively, in unconfused regions in the ecliptic plane. Saturation affects photometry of sources brighter than approximately 8.1, 6.7, 3.8 and -0.4 mag at 3.4, 4.6, 12 and $22\ \mu\text{m}$, respectively. We use only W_1 and W_2 bands in the current work because of the low sensitivities of W_3 and W_4 bands and the poor angular resolution of the W_4 band.

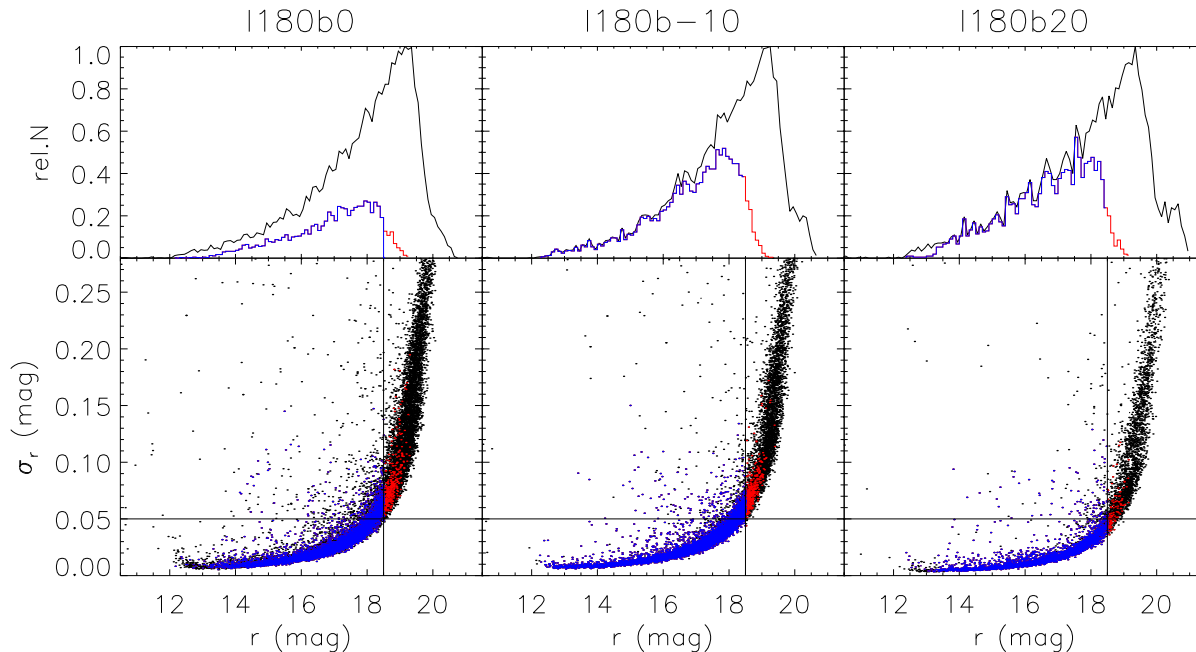


Figure 1. Distributions of relative star count (upper panels) and (formal) r -band photometric measurement uncertainties (lower panels) as a function of r -band magnitude for three fields, each of $1^\circ \times 1^\circ$, for lines of sight $l = 180^\circ$ and $b = 0, -10$ and $+20^\circ$, respectively. The black lines and dots represent all XSTPS-GAC sources in the fields, whereas those represented by blue plus red lines and dots are sources with matching 2MASS and WISE photometry. Only sources represented by blue lines and dots are included in the final sample analyzed in the current work.

2.4 Sample selection

We select sources in the XSTPS-GAC with matching targets in the 2MASS and WISE catalogs. We use the Centre de Données astronomiques de Strasbourg (CDS) XMatch Service¹ to cross-match the sources by position on the sky. The matching radius is set to $1.5''$, with which the fraction of multiple matches is less than 0.01% for the whole GAC survey area. About 90% of the cross-identified sources have a matching distance between the XSTPS-GAC and 2MASS/WISE positions smaller than $0.5''$. The combined XSTPS-GAC/2MASS/WISE catalog contains about 30 million sources. As mentioned before, XSTPS-GAC sources with $r < 18.5$ mag typically have photometric errors smaller than 0.05 mag (c.f. Fig. 1). To select sample stars from the combined XSTPS-GAC/2MASS/WISE catalog, we require that the sources must have r band magnitude $r < 18.5$ mag and are detected in all bands, i.e. XSTPS-GAC g, r, i ; 2MASS J, H, K_s ; and WISE $W1, W2$. The requirements lead to approximately 27 million sources ($\sim 90\%$) in the combined catalog.

For three selected lines of sight, the distributions of r -band star count as well as (formal) photometric measurement uncertainties of XSTPS-GAC sources, those with matching 2MASS and WISE photometry (blue plus red lines and dots), and those included in the final sample (blue lines and dots only) are illustrated in Fig. 1 as examples. As the Galactic latitude decreases, the number of star counts increases, yet the fraction of XSTPS-GAC with matching 2MASS and WISE photometry becomes smaller. At the Galactic plane ($b = 0^\circ$, left panel of Fig. 1), only $\sim 45\%$ of XSTPS-GAC sources have near- and mid-IR magnitudes. The

fraction also decreases for fainter sources. There is a steep decrease around $r = 18.5$ mag. This is not surprising given that the survey depth of XSTPS-GAC is deeper than those of 2MASS and WISE, at least for not so heavily reddened regions. The XSTPS-GAC/2MASS/WISE combined catalog has a typical completeness limiting r -magnitude slightly deeper than 18 mag. Main-sequence stars with 2MASS $K_s < 14.3$ have distances smaller than approximately 1–2 kpc (Berry et al. 2012), while dwarfs with XSTPS-GAC $r < 18.5$ mag can be as far as 4 kpc (Liu et al. 2014). As in the case of the three optical bands of XSTPS-GAC, for the three 2MASS near-IR and two WISE mid-IR bands, the errors of sources with (formal) reported photometric errors less than 0.02 mag are reset to 0.02 mag.

3 METHOD

In this work we adopt a similar method originally proposed by Berry et al. (2012), by applying SED fitting to multi-band data from the XSTPS-GAC, 2MASS and WISE combined catalog. There are two empirical results that form the basis of this method: the stellar locus in the multi-dimensional colour space and the shape of dust extinction curve being depicted by a one-parameter function. We begin introducing our method by first describing those two empirical results.

3.1 Reference stellar locus

The nearly blackbody emission spectra of stars place them predominantly along a line in optical and infrared colour-colour space. The broad band colours of a star are almost entirely determined by the

¹ <http://cdsxmatch.u-strasbg.fr/xmatch>

star’s effective temperature, metallicity, and surface gravity. Furthermore, the optical and infrared colours are largely determined by the effective temperature and hardly affected by the surface gravity and metallicity (Covey et al. 2007; Ivezić et al. 2007; High et al. 2009). As a consequence, in the treatment below, we have neglected the effects of the latter two parameters.

Covey et al. (2007) calculate the running-median of colours for a sample of 600,000 stars, observed by the SDSS and 2MASS in the *ugrizJHK_s* photometric system. The extinction of sample stars are estimated using the SFD maps for $A_r < 0.2$ mag. They present the stellar locus as a function of colour ($g - i$), for the range $-0.25 < (g - i) < 4.50$. The results are used by Berry et al. (2012) as an empirical SED library and adopted by High et al. (2009) as the standard empirical stellar locus. Most recently, Davenport et al. (2014) present the fiducial main sequence stellar locus traced by 10 photometric colors observed by SDSS, 2MASS, and WISE. Because the photometric catalog of XSTPS-GAC is an entirely new data set and Covey et al. (2007) lack the information of mid-IR colours, we have recalculated the empirical stellar locus for our own XSTPS-GAC, 2MASS and WISE combined multi-band catalog. We first define a “high-quality reference sample of (essentially) zero extinction” by imposing the following criteria: a line-of-sight Galactic extinction A_r less than 0.075 mag as given by the SFD map and photometric errors in the individual band ($g, r, i, J, H, K_s, W1, W2$) smaller than 0.05. The criteria are more restrictive than those of Covey et al. (2007) and Davenport et al. (2014). The cuts lead to a reference sample consisting of 132,316 stars. As in Covey et al. (2007), we assume the ($g-i$) colour as the independent variable for the stellar locus. Given the above strict cut on the upper limit of extinction, we have ignored the effect of reddening for the reference sample.

The colour-colour diagrams for our reference sample are plotted as density contours in Fig. 2. The abscissa is the chosen independent variable ($g - i$) while the ordinates include the seven colours from adjacent bands, ($g - r$), ($r - i$), ($i - J$), ($J - H$), ($H - K_s$), ($K_s - W1$), and ($W1 - W2$). The contours are shown on a logarithmic scale. Fig. 2 shows that the stellar locus are very compact. The locus for the IR bands, ($H - K_s$), ($K_s - W1$), and ($W1 - W2$) appear to be slightly broader. This is because of the small colour ranges of the ordinate. We notice that our multi-band catalog, ($g - i$) spans a range from about -0.5 to 4 . We then calculate the median values for each colour of adjacent bands in individual ($g - i$) bins ranging from -0.5 to 3.8 . For $0.2 < (g - i) < 3.48$, the bin width is 0.02 mag, and 0.1 mag outside the range considering the low stellar density. The median values are represented by red crosses in Fig. 2. Overplotted in blue are spline fits to the median values. Even a 5th order polynomial can not fit the data well, in particular near the blue and red edges of the stellar locus. The adopted spline function fits the data very well, with typical residuals ~ 0.01 mag and less than 0.02 mag in general (c.f. the right upper panel of Fig. 2). The resultant fits are used to generate a standard SED library adopted in the current work. For comparison, we also plot in Fig. 2, the locus obtained by Davenport et al. (2014; cyan dashed lines) colours of the three optical and three near-IR bands. The agreement is very good, although some small differences are clearly visible towards redder colors.

Except for ($J - H$) and ($W1 - W2$), one of the most significant features of the standard locus plotted in Fig. 2 are their monotonic behavior. Some locus, including those of ($g - r$), ($r - i$), ($J - H$) and ($W1 - W2$) exhibit a change of slope at around ($g - i$) ~ 1.95 mag. As shown by previous studies, (Finlator et al. 2000; Hawley et al. 2002; Covey et al. 2007; Jurić et al. 2008; High et al.

2009), blueward of this break point, evolved and main-sequence A- to K-type stars dominate the population, whereas redward of the point M-type dwarfs take over. The metallicity dependence of the disk main-sequence stars blueward of this break point of locus is small. The metallicity variations of M dwarfs in the disk could perturb the kink region of the observed locus (High et al. 2009).

The standard SED library generated from the reference stellar locus can not be applied for blended or binaries, which may possess quite different SEDs (Richards et al. 2001; Smolčić et al. 2004; Eisenstein et al. 2006; Berry et al. 2012). Fortunately as already discussed by Berry et al. (2012), those stars consist only a minority (Finlator et al. 2000; Jurić et al. 2008; Liu et al. 2014) and can generally be detected and excluded by their large values of minimum χ^2 in the process of SED fitting.

3.2 Extinction law

Cardelli et al. (1989) derive a $R(V)$ -dependent Galactic extinction law for the wavelength range $0.125 \leq \lambda \leq 3.5 \mu\text{m}$. Slightly different results are obtained by O’Donnell (1994) for the near-UV to the optical wavelength range ($0.303 \leq \lambda \leq 0.909 \mu\text{m}$). A new extinction law from the UV to the IR ($0.1 \leq \lambda \leq 3.4 \mu\text{m}$) is presented by Fitzpatrick (1999). Following the releases of survey data of the SDSS in the optical and other surveys in the IR, such as 2MASS in the near-IR and GLIMPSE (The Spitzer Galactic Legacy Infrared Midplane Survey Extraordinaire; Benjamin et al. 2005) in the mid-IR, number of studies have been carried out investigating the extinction law in the optical and IR wavelength ranges for different regions and environments of the Milky Way (e.g. Indebetouw et al. 2005; Jiang et al. 2006; Flaherty et al. 2007; Nishiyama et al. 2009; Fitzpatrick & Massa 2009; Gao et al. 2009; Schlafly & Finkbeiner 2011; Chen et al. 2013). Using SDSS and 2MASS data, Berry et al. (2012) constrain the shape of the extinction curve and find that their result is compatible to that of Fitzpatrick (1999) but not of O’Donnell (1994). Berry et al. (2012) recommend the fixed R_V value as 3.0 and a corresponding interstellar extinction coefficient $C_\lambda \equiv A_\lambda/A_r$ of 1.400, 0.759, 0.317, 0.200 and 0.132 for g, i, J, H, K_s bands, respectively.

More recently, Yuan et al. (2013) combine data from the SDSS, GALEX (Galaxy Evolution Explorer; Martin et al. 2005), 2MASS and WISE, and study the extinction law of the Milky Way from the far UV to the mid-IR using the star pair technique. The technique pairs stars suffering from high extinction with their twins that suffer from almost nil extinction but otherwise have almost identical stellar parameters as given by spectroscopic observations and analyses. Using this technique, Yuan et al. measure the dust extinction for thousands of Galactic stars and derive the empirical reddening coefficients for photometric bands ranging from the UV to the mid-IR. The method has the advantages that it is straightforward, model-free and applicable to the majority of stars. For the optical and IR bands, they obtain values of $C_\lambda = 1.42, 0.74, 0.31, 0.19, 0.13, 0.082$ and 0.065 for $g, r, J, H, K_s, W1$ and $W2$ bands, respectively, very similar to those of Berry et al. (2012). Considering that the current work use the same optical and IR data set as Yuan et al. (2013) and the fact that the stellar locus obtained here are almost identical to those derived using data from the SDSS (Covey et al. 2007; Davenport et al. 2014), we have therefore simply adopted the extinction coefficients given by Yuan et al. (2013) of a fixed R_V value of 3.1.

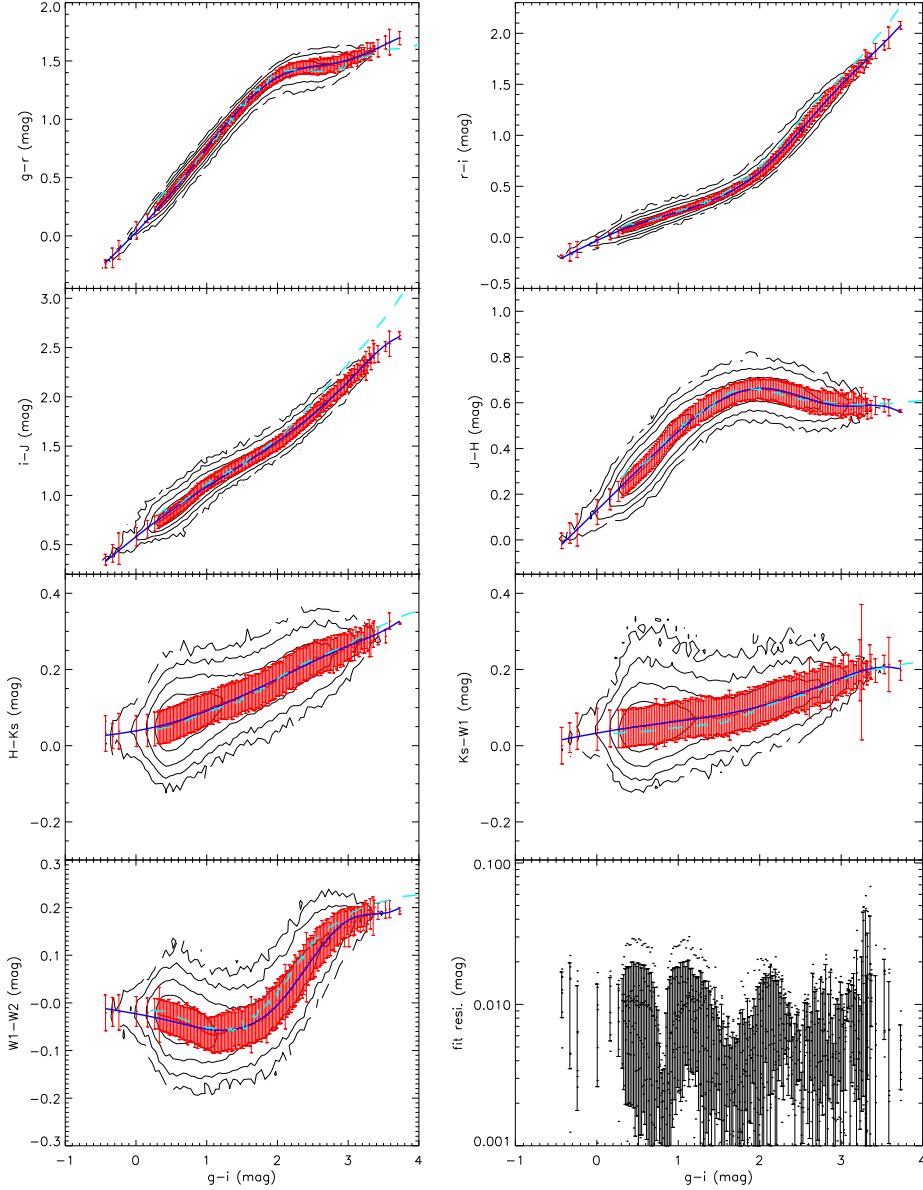


Figure 2. Colour-colour diagrams of 132,316 reference stars of essentially zero interstellar extinction selected from the combined catalog of the XSTPS-GAC, 2MASS and WISE surveys with high quality photometry. The contours are on a logarithmic scale. Red pluses and associated errorbars represent the median values and standard deviations of the colour plotted as ordinate for the individual bins of $(g - i)$ as abscissa. The blue lines are spline fits to the median values. Also overplotted for comparison are stellar locus from Davenport et al. (2014). The bottom-right panel shows the residuals of spline fits with the errorbars indicating the scatters of residuals of the seven colours.

3.3 Extinction determinations

Our procedure to derive extinction by SED fitting is very similar to that of Berry et al. (2012). With the reference stellar locus and extinction law fixed, assuming a SED library index t [in our case, we use $(g - i)_0$] and a r -band extinction A_r , we can apply a simple

model to simulate the observed colour of bands λ_1 and λ_2 for a given star (Berry et al. 2012):

$$c_{sim} = c_{sl}[(g - i)_0] + (C_{\lambda_1} - C_{\lambda_2})A_r \quad (1)$$

where c_{sim} is the simulated colour, $(g - i)_0$ describes the position of the star on the reference stellar locus, c_{sl} is the colour predicted by

the reference stellar locus for $(g - i)_0$, $C_{\lambda 1}$ and $C_{\lambda 2}$ are extinction coefficients for bands $\lambda 1$ and $\lambda 2$ given by the assumed extinction law. With $(g - i)_0$ and A_r as free parameters, we can then model the seven observed colours formed by adjacent bands (e.g. $(g - r)$, $(r - i)$, etc.) of our data set. Similar to Eq. (3) of Berry et al. (2012), we define

$$\chi^2 = \frac{1}{5} \sum_{i=1}^7 \left(\frac{c_{obs}^i - c_{sim}^i}{\sigma_i} \right)^2 \quad (2)$$

where c_{obs}^i and c_{sim}^i are the i th observed and simulated colours ($i=1, 2, \dots, 7$), and σ_i is the colour measurement uncertainty computed by adding the photometric errors in quadrature. The best-fit model is then obtained by minimizing χ^2 .

The optimization to minimize χ^2 , is carried out by running a pseudo A_r ranging from 0 to 10 in step of 0.02 mag and all index value $i \equiv (g - i)_0$ of our reference SED library. The procedure yields best fit values of A_r , as well as $(g - i)_0$ for the star of concern. In doing so we have ignored the possible contributions to colour uncertainty σ_i produced by the finite width of the empirical library SED, a simplification also made by Berry et al. (2012). The errors of the best fit values of A_r and $(g - i)_0$ are calculated from the ellipse fitting parameters of the χ^2 surface defined by $\chi^2 < \chi_{min}^2 + 6.17$, see Berry et al. (2012) for more information.

3.4 Extinction and photometric parallax of open clusters

Distances of stars in our sample are calculated using the derived best-fit values $(g - i)_0$ using a photometric parallax relation, such as that given by Jurić et al. (2008) and Ivezić et al. (2008). This is a simplified approach. In addition to ignoring possible binarity and blending, the approach also ignores the fact that stars have different metallicities and ages, and assumes that all stars are main-sequence dwarfs. Accordingly, the best-fit parameters, $(g - i)_0$ and A_r returned by the procedure could occasionally be totally wrong. We have made a series of tests to check the reliability of our method. As a first test we apply the method to a few well studied stellar clusters.

We select two open clusters in the GAC region: M 67 (NGC 2682) at high Galactic latitude ($l = 215.696$ deg, $b = +31.896$ deg) with low dust extinction (Xin & Deng 2005) and the other is M 35 (NGC 2168) at low Galactic latitude ($l = 186.591$ deg, $b = +02.191$ deg.) with high dust extinction (Wu et al. 2009). Basic parameters of those two clusters, shown in Table 1, are well documented in the literature, such as the recently published papers by Kalirai et al. (2003); Yadav et al. (2008); An et al. (2008); Geller et al. (2010).

The sources of M 67 are selected using the cross-match between our sample and the catalog of Yadav et al. (2008). We use sources with a proper-motion membership probability larger than 60% in their catalog and obtain 403 stars. Members of M 35 are selected by matching with the catalog of Geller et al. (2010). We select stars with a radial-velocity membership probability larger than 50% and obtain 282 stars. We then apply our method to the selected stars and obtain best-fit values of $(g - i)_0$ and A_r for each member star in the two clusters. Regarding our new stellar locus are in good agreement with those deduced from the SDSS data (Covey et al. 2007; Davenport et al. 2014), distances of individual stars are calculated using two photometric parallax relations, one from the ‘‘bright’’ relation of Jurić et al. (2008) and another from Ivezić et al. (2008). The ‘‘bright’’ relation is given in terms of $(r - i)$, which can be converted from the best-fit value of $(g - i)_0$ using the

reference stellar locus:

$$M_{r,J08} = 3.2 + 13.30(r - i) - 11.50(r - i)^2 \\ 5.40(r - i)^3 - 0.70(r - i)^4.$$

The relation of Ivezić et al. (2008) is given in terms of $(g - i)_0$ colour:

$$M_{r,J08} = \Delta M_r([\text{Fe}/\text{H}]) - 5.06 + 14.32(g - i) \\ - 12.97(g - i)^2 + 6.127(g - i)^3 - 1.267(g - i)^4 \\ + 0.0967(g - i)^5,$$

where $\Delta M_r([\text{Fe}/\text{H}]) = 4.50 - 1.11[\text{Fe}/\text{H}] - 0.18[\text{Fe}/\text{H}]^2$ is the metallicity correction. The distance d , in units of parsec, of a star with an intrinsic absolute magnitude M_r , can be calculated from the standard relation, $d = 10^{0.2(r_0 - M_r) + 1}$, where $r_0 = r - A_r$ is the dereddened magnitude of the star in r band. In Fig. 3, we plot distances calculated from the two photometric parallax relations for member stars of the two clusters. The black horizontal lines in the diagram denote the reference distances adopted for the two clusters: 0.89 kpc for M 67 and 0.91 kpc for M 35. Both relations seem to yield satisfactory results for members of the two clusters except for a few outliers. There is a small systematic offset between the distances yielded by the two relations, those deduced using the Jurić et al. (2008) relation (d_{J08}) are about 0.1 kpc smaller than values derived from the Ivezić et al. (2008) relation (d_{I08}). Fig. 3 also shows there is a linear trend between d_{J08} and $(r - i)_0$ – redder stars have smaller distances. Such a trend is not so obvious for d_{I08} . In this study, we will adopt distances calculated from the best-fit $(g - i)_0$ colour using the Ivezić et al. (2008) parallax relation, which is applicable for a wide $(g - i)_0$ colour range from 0.0 to about 4.0 (Ivezić et al. 2008). For the term of metallicity correction in the Ivezić et al. (2008) relation, since almost all stars in our sample are from the disk, we have adopted a universal $[\text{Fe}/\text{H}] = -0.2$ for all stars, the median metallicity for stars targeted by the LSS-GAC (Xiang et al. 2014, in preparation). As shown by Xiang et al. (2014) most stars targeted by the LSS-GAC have $[\text{Fe}/\text{H}]$ between -0.7 and 0.2 dex. For a star with an extreme value of metallicity ($[\text{Fe}/\text{H}] = -0.7$ or $+0.2$ dex), adopting the universal $[\text{Fe}/\text{H}]$ value of -0.2 dex will lead to a metallicity correction term $\Delta M_r([\text{Fe}/\text{H}])$ offset by about ± 0.45 mag, and consequently a distance offset by about ± 0.2 kpc, or about 20% error for a star at 1 kpc.

Fig. 4 shows the distribution of distances d and extinction A_r , deduced for individual stars relative to the reference values for the two clusters. Also overplotted are Gaussian fits to the distributions. The good fits show that our method is capable of yielding reliable parameters for most stars. The absence of stars on the left of the distribution of $\Delta A_r = A_{r,\text{fit}} - A_{r,\text{ref}}$ in the case of M 67 is due to the very low extinction of this cluster ($A_{r,\text{ref}} = 0.093$ mag) and the fact that negative values of extinction yielded by the fitting process are deemed unphysical and therefore discarded. We also note that there is a systematic offset in the distributions of distances, in the sense that distances yielded by the photometric parallax relation are on average about 0.07 kpc larger than the reference values. For extinction, no obvious systematic offsets are seen. The broader distributions of M 35 compared to those of M 67 may indicate that higher extinction has an impact on both distance and extinction estimates.

3.5 Test with fiducial stars and mock catalogs

In this Section, we perform further tests on the reliability and accuracy of our algorithm in recovering the reddening and distances

Table 1. Basic parameters of M 67 and M 35.

	distance (pc)	$(m - M)_0$ (mag)	age	[Fe/H]	$E(B - V)$
M 67	890 ^a	9.56 – 9.72 ^b	3.5 – 4.8 Gyr ^b	+0.03 ± 0.01 ^c	0.041 ^d
M 35	912 ⁺⁷⁰ ₋₆₅ ^e	9.80 ± 0.16 ^e	180 Myr ^e	-0.21 ^e	0.20 ^e

Reference: *a*: An et al. (2008); *b*: Yadav et al. (2008); *c*: Randich et al. (2006); *d*: Taylor et al. (2008); *e*: Kalirai et al. (2003).

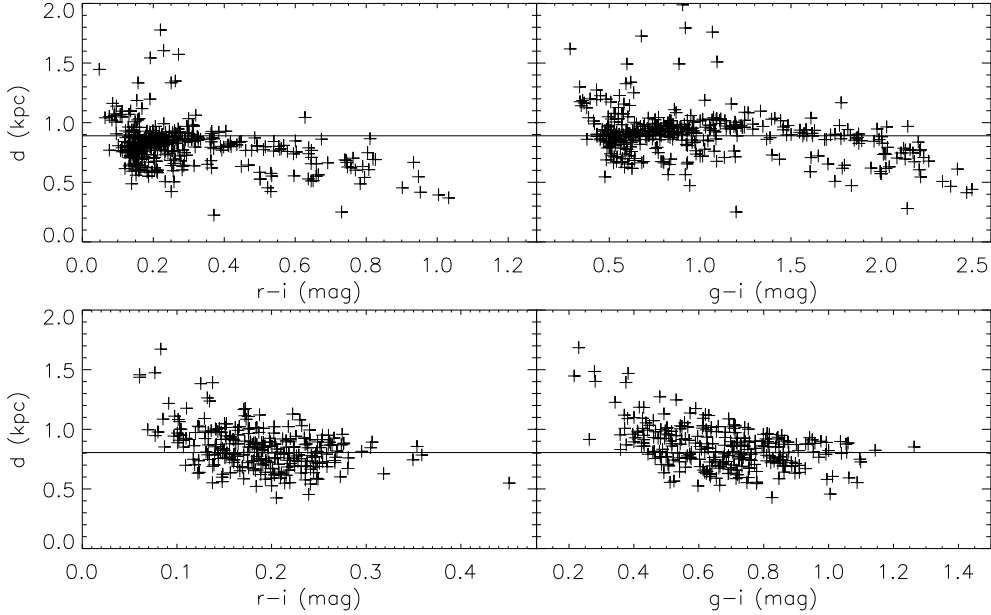


Figure 3. Distances deduced for member stars of M 35 (bottom panels) and M 67 (upper panels), using the “bright” relation of Jurić et al. (2008; left panels) and that of Ivezić et al. (2008; right panels). The horizontal lines denote reference distances adopted for the two clusters, 0.89 kpc for M 67 and 0.91 kpc for M 35.

by applying the method to simulated fiducial stars, as well as to mock photometric catalogs created with the Besançon Galaxy model (Robin et al. 2003, 2012).

First we simulate a fiducial star with different intrinsic colours $(g - i)_0 = 0.50, 1.95$ and 2.50 , representing stars located on the blue, “knee”, and red positions of the stellar locus (c.f. Fig. 2). Three sets of photometric errors are assigned using Gaussian distributions of widths 0.02, 0.05 and 0.08 mag, respectively. The value of A_r is fixed at 1.5 mag. Photometric magnitudes in the 8 bands, $g, r, i, J, H, K_s, W1$ and $W2$ are generated from the reference SED library (c.f. Fig. 2) using a random r -band reference magnitude r_0 , ranging from 12 to 19 mag. Photometric errors of individual magnitudes of the eight bands are generated independently. Our algorithm is then applied to the resultant “observed” colours to derived the best-fit values of $(g - i)_0$ and A_r . For each fiducial star, we generate the magnitudes randomly and calculate the best-fit parameters $(g - i)_0$ and A_r of minimum χ^2 for 10,000 times. Fig. 5 shows distributions of the best-fit parameters in the $(g - i)_0$ and A_r plane, and histograms of best-fit values of A_r . The top, middle and bottom panels correspond to the three simulated cases of intrinsic colours, i.e. $(g - i)_0 = 0.5$ (a blue star), 1.95 (a star near the “knee” of the stellar locus), and 2.50 (a red star), respectively. In each row, the three panels refer to the three cases of photometric errors: 0.02, 0.05 and 0.08 mag for (a), (b) and (c), respectively. As noticed by Berry et al. (2012) earlier, the covariance of the best-fit values of

$(g - i)_0$ and A_r is larger for a blue star than a red one. For stars with high photometric accuracy ($\sigma_i = 0.02$), the algorithm recovers the values of $(g - i)_0$ and A_r perfectly, a blue, “knee” or red star, regardless. For a blue or red star, the χ^2 distribution always possesses only one peak, even for $\sigma_i = 0.08$ mag. The best-fit algorithm is quite robust in these two cases where increasing the photometric errors simply leads to larger uncertainties of the results. However, for a “knee” star, the best fit A_r distribution becomes quite complicated, showing multiple peaks for photometric errors larger than 0.05 mag. For such stars, results yielded by the method should be treated with caution.

Next we test our algorithm using mock catalogs generated with the Besançon Galactic stellar population synthesis model (Robin et al. 2003, 2012). The Besançon Galaxy model is based on a scenario of the formation and evolution of the Milky Way. It simulates the stellar contents of the Galaxy with four distinct stellar populations: a thin disc, a thick disc, a bulge and a spheroid. It also takes into account the presence of a dark halo and a diffuse component of the interstellar medium. To test our method, we create artificial data by adding manually extinction values to intrinsic magnitudes generated by the model. Fig. 6 shows an example of our test, for a one squared degree field centered at $(l, b) = (180.00, -10.00)$. Since the current Besançon model does not include $W1$ and $W2$ bands, we use the IRAC [3.6] and [4.5] bands as surrogates since they are very close. We assume an

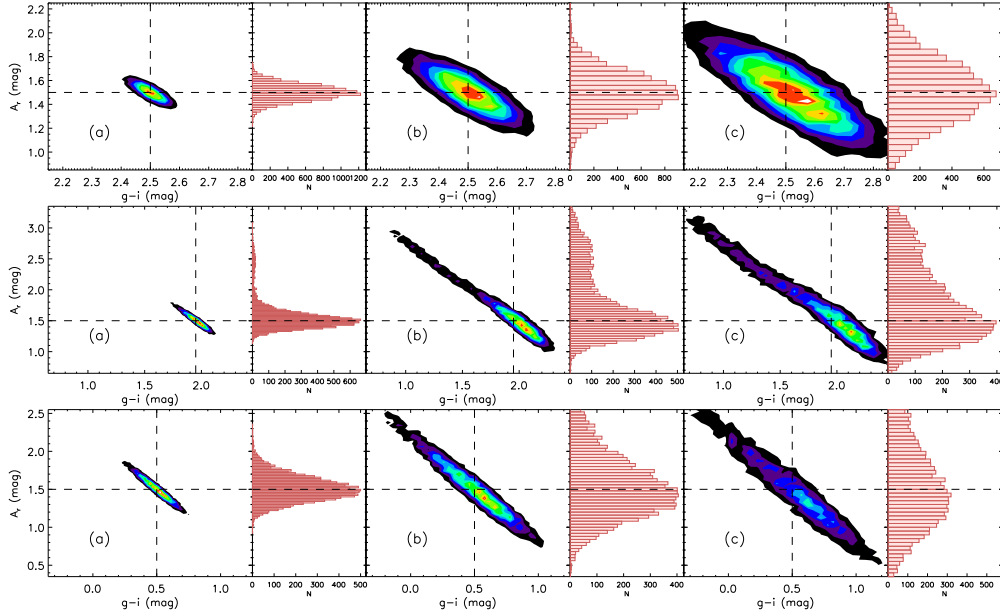


Figure 5. Monte Carlo simulations for three fiducial stars of intrinsic colours $(g - i)_0 = 2.5$ (top panels), 1.95 (middle panels), and 0.5 (bottom panels). The pseudo colour image in each panel shows distribution of the best-fit parameters in the $(g - i)_0$ and A_r plane. Also shown to the right of each panel is a histogram of the best-fit values of A_r . For each row, (a), (b) and (c) from left to right the three panels refer respectively to the results of the three assumed cases of photometric errors, 0.02, 0.05 and 0.08 mag.

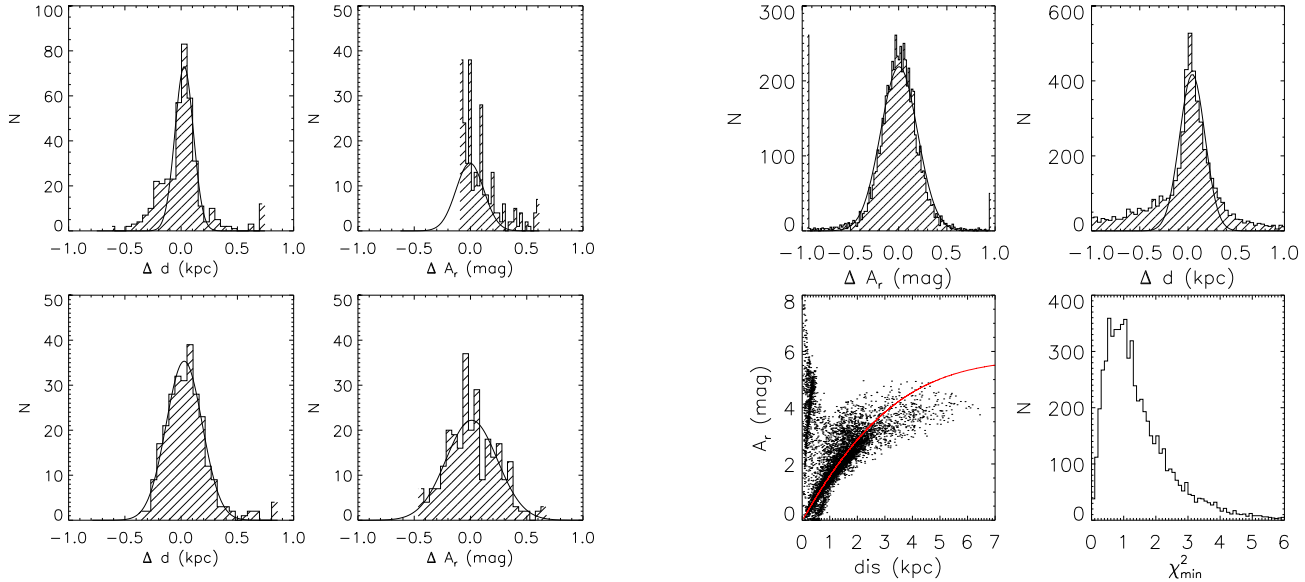


Figure 4. Distributions of offsets of values of distance d (left panels) and extinction A_r (right panels) relative to the reference values for M35 (bottom panels) and M67 (upper panels). Also overplotted are Gaussian fits to the distributions.

extinction gradient of 2.0 mag/kpc in V band. The completeness limit is set to 19 mag in r band and photometric errors to 0.05 mag for all bands. Note that the Besançon model computes the photome-

Figure 6. Test results for a one squared degree field simulated with Besançon model. *Upper left:* Histogram distribution of differences of A_r extinction values deduced from our fitting algorithm and those assumed in the model. *Upper right:* Same as upper left but for stellar distances. *Lower left:* A_r plotted against distance. Values recovered by our fitting algorithm are represented by dots. The red solid line is the artificial extinction assumed in the Galactic model. *Lower right:* Histogram of minimum χ^2 values of fits.

try using stellar atmosphere models (Basel 3.1) from Lejeune et al. (1997) and Lejeune et al. (1998). The Basel 3.1 stellar library is different from our empirical reference stellar library (Fig. 2). So we replace our reference stellar locus by the Basel 3.1 stellar library for consistency. We also assume the empirical extinction law of Mathis & Cardelli (1990), to be consistent with the Besançon model.

The test results are presented in Fig. 6. The lower left panel of Fig. 6 plots the best-fit distances versus values of extinction recovered by our algorithm. The overplotted red line delineates the increase of extinction as a function of distance assumed in the Galactic model and the black dots are the best-fit values of extinction and distance for individual stars of the mock catalogue. For most of the stars, the best-fit values trace closely the model ones. Those well behaving stars are in fact dwarfs. There are however a bunch of stars in the upper left parts of the diagram, i.e. stars at small distances yet having very high values of extinction. Those are giant stars. For giants, our algorithm has grossly underestimated their distance. Giants have intrinsic colours almost identical to dwarfs. However, they are intrinsically much brighter and therefore for a magnitude limited sample, most giants are located at much further away than dwarfs. The distributions of differences of our best-fit and model values are well represented by a Gaussian, for the cases of both distance and extinction (top panels of Fig. 6). For extinction and distance, the average value and dispersion of the differences are respectively -0.006 ± 0.16 mag and -0.05 ± 0.13 kpc. The lower right panel of Fig. 6 shows the resulting minimum χ^2 distribution of the algorithm. As expected, the χ^2 distribution peaks at unity. The distributions of distance differences and χ^2 values are skewed because of the underestimated distances for giant stars. The test shows that our method can successfully recover the extinction values and distances for dwarfs but underestimates the distances of giants. The simulations also show that the contamination of giant stars in the XSTPS-GAC sample is quite small, probably less than 10% (Liu et al. 2014).

The above test of fiducial stars yields residuals of extinction of 0.002 ± 0.1 , 0.01 ± 0.2 and 0.02 ± 0.3 mag for photometric errors of 0.02, 0.05 and 0.08 mag, respectively, whereas the test with Besançon model yields residuals of -0.006 ± 0.16 mag and 0.045 ± 0.13 kpc for extinction and distance, respectively. Both tests thus show that except for giants our method and implementation of the χ^2 minimization algorithm is capable of yielding accurate parameters for most stars. Values of reddening together with distances for individual dwarfs can be accurately recovered.

4 RESULT

4.1 χ^2 distribution

Our algorithm is applied to the subset of the XSTPS-GAC, 2MASS and WISE combined multi-band photometric catalog (c.f. Section 2.4). We present our results by first discussing the distribution of minimum χ^2 values of best-fit parameters, χ_{\min}^2 . Fig. 7 shows the distributions of stars located at different ranges of Galactic latitude, as well as for stars with different ranges of photometric errors. All distributions peak around unity. As Galactic latitude decreases, stars begin to suffer from higher extinction, have higher photometric errors, and are contaminated by more giants, all these make the χ_{\min}^2 distribution shifting toward larger values. For the three regions of different Galactic latitude range plotted in the left panel of Fig. 7, the 68.3% cut of the accumulative distributions correspond

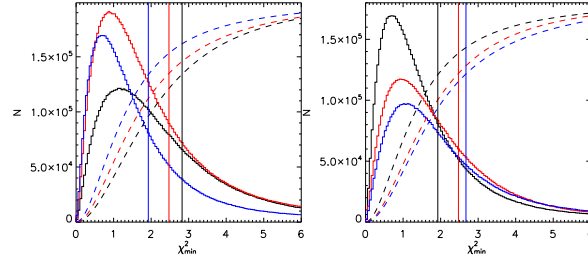


Figure 7. Distributions (solid curves) and accumulative distributions (dashed curves) for minimum χ^2 values of best-fit parameters for sample stars in different ranges of Galactic latitude (left panel; *Black*: $|b| < 5$ deg; *Red*: $5 \leq |b| \leq 15$ deg; *Blue*: $|b| > 15$ deg), and for stars with different ranges of mean photometric errors (right panel; *Black*: $\bar{\sigma} < 0.05$ mag; *Red*: $0.05 \leq \bar{\sigma} \leq 0.08$ mag; *Blue*: $\bar{\sigma} > 0.08$ mag). The three vertical lines refer to the 68.3% cut of the corresponding cumulative distributions.

to χ_{\min}^2 values of 2.85, 2.45 and 1.95 for regions of $|b| > 15$ deg, $5 \leq |b| \leq 15$ deg and $|b| < 5$ deg, respectively.

The right panel of Fig. 7 shows χ_{\min}^2 distributions for groups of stars of different ranges of photometric errors. We divide the sample into three groups by the average values of photometric errors of the eight bands: $0.02 \leq \bar{\sigma} < 0.05$ mag, $0.05 \leq \bar{\sigma} \leq 0.08$ mag and $\bar{\sigma} > 0.08$ mag, representing in sequence stars of most to least reliable photometry. Note that we have imposed an r -band limiting magnitude cut $r < 18.5$ mag when defining the sample (c.f. Section 2.4), implying that while most stars have r -band errors less than 0.05 mag, there are some stars in the sample whose r -band or other bands errors are larger than 0.08 mag. Also note that we have set the minimum photometric errors to 0.02 for all eight bands to account for possible systematic (calibration) uncertainties. Fig. 7 clearly shows that as photometric errors increase, the χ_{\min}^2 distribution shifts to larger values. The χ_{\min}^2 values corresponding to the 68.3% cut of the accumulative distributions are 1.95, 2.45 and 2.70, respectively, for the three groups of stars of increasing mean photometric errors.

Stars with $\chi_{\min}^2 < 2.0$ are included in our catalog of final results. The catalog thus contains more than 68.3% stars located at high Galactic latitudes $|b| > 15$ deg and the same fraction of stars of mean photometric errors $\bar{\sigma}$ less than 0.05 mag. The catalog consists of more than 14.6 million stars. In the catalog, stars with mean photometric errors $0.02 \leq \bar{\sigma} < 0.05$ mag are flagged by “A” for most reliable results, stars with $0.05 \leq \bar{\sigma} \leq 0.08$ mag by “B”, and those with $\bar{\sigma} > 0.08$ mag by “C” for least reliable results. For convenience of analysis below, we define Sample A that contains all stars with flag “A” in the catalog of final results and Sample C that includes all stars in the whole catalog of final results. Note that Sample C does not only include the stars with flag “C” but also with “A” and “B” as well.

4.2 The three dimensional distribution of dust

The catalog of final results, containing best-fit A_r and distance parameters for over 11 million stars, is publicly available online, along with the reference stellar locus library². As illustration, in Fig. 8 the values of extinction are plotted against distances for stars in the final catalog for three sample $1^\circ \times 1^\circ$ fields centered at

² <http://162.105.156.249/site/Photometric-Extinctions-and-Distances>.

$l = 180^\circ$ and $b=0^\circ, -10^\circ$ and 20°). Not surprisingly, most stars of Sample A are located at closer distances. This is because Sample A stars have higher photometric accuracy, and are on average brighter and thus at smaller distances. The dashed line in each panel marks the “boundary” between dwarfs and giants (Berry et al. 2012). Stars above the dashed lines are likely giants with grossly underestimated distances (c.f. Section 3.5 and Fig. 6). There are approximately 2 million stars above the dash lines in total, less than 20% of the whole final sample. The same criteria for the selection of giant candidates with Berry et al. (2012, Section. 3.1.5) is adopted for the entire catalog of the final results and 75,541 stars are selected out as giant candidates. These candidates are cross-matched with the LSS-GAC data (Yuan et al. 2014, to be submitted) and we obtain the basic parameters, T_{eff} , $[Fe/H]$, $\log g$, for 4,929 stars of them. About 80% of the 4,929 stars have $\log g$ smaller than 4.0 and have a peak at $\log g = 2.6$, implying that the giant candidates selection is quite reliable. We mark these candidates with an additional flag as “G” in the final catalog.

In principle, one should see that extinction increases with distance. Such a trend is not so obvious for high latitude fields, given the low extinction of those fields and the fact that for those fields most stars are likely behind the dust layer. On the other hand, the trend is very significant for low latitude fields. As pointed out earlier, in the plane, most of the stars are embedded within the dust layers rather than behind it. Thus if one uses the total extinction from a 2D extinction map (such as that of SFD) to deredden a disk star, it is quite likely that the extinction has been overestimated. The analyses of Arenou et al. (1992) and Chen et al. (1999) assumed that extinction as a function of distance can be approximated by a 4th order polynomial, $E(B - V) = a_1 r + a_2 r^2 + a_3 r^3 + a_4 r^4$. However studies including the current one (Marshall et al. 2006; Chen et al. 2013; Schultheis et al. 2014) have shown that the relation between extinction and distance is quite complicated and varies from field to field. The results presented in Fig. 8 illustrate well the power of a 3D extinction map. Firstly, the extinction in the field $(l, b) = (180^\circ, 0^\circ)$ increases with distance up to a distance of ~ 4 kpc, while for the field $(l, b) = (180^\circ, 20^\circ)$ the extinction stops increasing at a distance of only 0.3 kpc. The results thus indicate a scale length and height of the dust layer of less than 4 kpc and 0.3 kpc, respectively. Secondly, measurements of the 3D dust distribution can be used to detect and trace dark clouds (Marshall et al. 2009; Schlafly et al. 2014). For example, in the field $(l, b) = (180^\circ, -10^\circ)$, one sees a dramatic increase of the extinction at a distance of about 0.2 kpc, which is in fact the location of the well known Taurus dark cloud (Straizys et al. 1992). Finally, a 3D extinction map of large sky area can trace the large structure of the dust distribution. Schultheis et al. (2014) find that the extinction first increases significantly at about 5–7 kpc and then decreases after 8 kpc toward the Galactic center. They suggest that there could exist a dust lane in front of the Galactic bar.

We employ a sliding window of width 450 pc with a step of 150 pc to obtain median value of extinction for each distance bin, excluding stars above the dashed lines, which are likely giants rather than dwarfs. The red lines in Fig. 8 plot the median extinction as a function of distance for the three fields after applying a boxcar smoothing of a width 450 pc. We group all stars in the catalog of final results into subfields of varying angular dimensions and calculate the median value of extinction in each sliding window, again excluding possible giants. The results are then used to derive extinction as a function of distance for each subfield. The adopted dimension of subfields (angular resolution) of the resultant map depends on latitude, as shown in the top right panel of Fig. 9.

For latitudes ranging $-15 < b < +10^\circ$ [denoted as region (a) in the panel], the stellar density is high enough to allow a high angular resolution of 3 arcmin. As the stellar density drops towards high Galactic latitudes, we reduce the resolution to 6 arcmin for $-35 \leq b \leq -15^\circ$ and $10 \leq b \leq 30^\circ$ [regions (b)], and to 9 arcmin for $b < -35^\circ$ and $b > 30^\circ$ [regions (c)]. For the high angular resolution regions, we require that there are at least 10 stars in each bin. Fig. 9 shows resultant 3D extinction maps for the entire GAC area surveyed by the XSTPS-GAC. The individual panels in the diagram present extinction maps by local dust grains in individual distance bins of length 400 pc ($0 - 0.4, 0.4 - 0.8, 0.8 - 1.2, 1.2 - 1.6, 1.6 - 2.0, 2.0 - 2.4, 2.4 - 2.8$ and $2.8 - 3.2$ kpc).

Fig. 9 represents the very first set of high angular resolution 3D extinction maps; covering about 6,000 deg² sky area of the GAC and spanning a distance range from 0 to 4 kpc. The data are available online from the aforementioned website. They are also available in electronic form at the CDS³. Table 2 provides an example of the format. Each row of Table 2 contains the information for one line of sight: Galactic coordinates along with the measured quantities for each distance bin A_r , and the respective uncertainties. The width of the distance bin is 150 pc.

Many interesting features are clearly visible in the dust distributions presented in Fig. 9, including the obvious disk warps. The features seen in Fig. 9 are consistent with previous studies (Schlegel et al. 1998; Dobashi et al. 2005; Froebrich et al. 2007) as well as with results from studies of the gas component [e.g. H I gas from Bajaja et al. (2005), CO gas from Dame et al. (2001)]. The large scale features in this sky region, such as λ -Ori around Galactic longitude and latitude $(189^\circ, -16^\circ)$, Orion A around $(205^\circ, -14^\circ)$, Orion B around $(213^\circ, -20^\circ)$, Auriga 1 around $(166^\circ, -8^\circ)$, Auriga 2 around $(180^\circ, -7^\circ)$, Taurus around $(170^\circ, -15^\circ)$, Camelopardalis 1 around $(150^\circ, 0^\circ)$, Camelopardalis 2 around $(158^\circ, 0^\circ)$, Monoceros around $(220^\circ, -5^\circ)$, Perseus around $(160^\circ, -20^\circ)$, Taurusextended 1 around $(180^\circ, -25^\circ)$, Taurusextended 2 around $(172^\circ, -35^\circ)$, Aries around $(160^\circ, -30^\circ)$, and Eridanus around $(190^\circ, -35^\circ)$, are clearly visible in the local volume, within 800 pc. Beyond this distance, we see mainly features from the Galactic thin disk. The contours overplotted in maps beyond 0.8 kpc show the distributions of integrated intensity of H I gas from Leiden-Argentina-Bonn (LAB) 21 cm H I emission survey (Kalberla et al. 2005). The features revealed by the dust are very similar to those of the gas. At distances beyond 3 kpc, our results become less reliable, due to less numbers of stars with high quality photometry available for extinction determinations. There is a notable empty patch around $l \sim 160^\circ$ and $b \sim 20^\circ$, due to abnormally large photometric errors of XSTPS-GAC.

Fig. 10 presents the extinction distribution in the Galactic disk plane from stars of vertical distances from the disk plane $|Z| < 150$ pc. It gives the extinction by local dust (in units of mag/kpc). The Sun is located at $X = 8$ kpc and $Y = 0$ kpc. A number of features are visible in the figure, including the local Orion arm that extends to about 800 pc at longitude of about 210° . The Perseus arm can be seen at distances of about 2–3 kpc. The well known Camelopardalis and Cassiopeia dust features are visible at longitudes between 130° and 150° beyond 800 pc. The position of the features are consistent with the location of young stars found in the Camelopardalis dust and molecular clouds (Straizys & Laugalys

³ The data is only available in electronic form at the CDS via anonymous ftp to cdsarc.u-strasbg.fr (130.79.128.5) or via <http://cdsweb.u-strasbg.fr/cgi-bin/qcat?J/A+A/>.

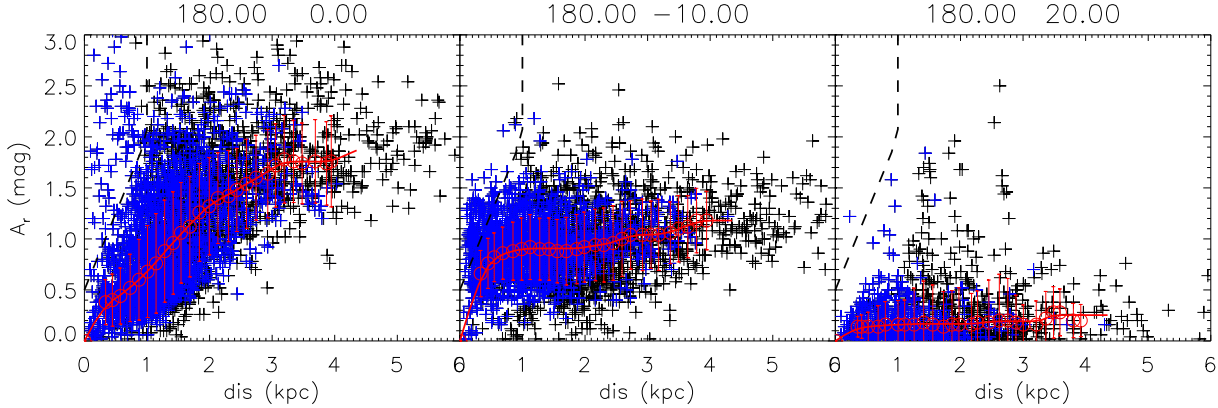


Figure 8. Extinction plotted against distance for stars in three example fields of $1^\circ \times 1^\circ$. The central Galactic longitude and latitude are marked on top of each panel. Black and blue symbols denote stars from Sample C and A, respectively. The red circles and errorbars are running medians and standard deviations of all data points of Sample C, excluding those above the dashed lines. The latter are most likely giants whose distances may have been grossly underestimated. The red lines smoothly delineate the median values after applying a boxcar smoothing. See text for more detail.

Table 2. Resulting extinction as a function of Galactic longitude, latitude, and distance.

l (deg)	b (deg)	$A_{r,0.0-4.35\text{kpc}}$ (mag)	$\sigma A_{r,0.0-4.35\text{kpc}}$ (mag)
-----------	-----------	----------------------------------	-----------------------------------------

Notes. For each position we provide the r band extinction, and the corresponding sigma for each distance bin starting from 0.0 to 4.35 kpc, with a step of 150 pc.

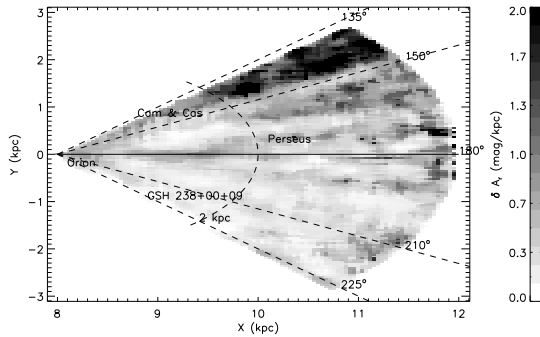


Figure 10. Distribution of differential extinction (in units of mag kpc^{-1}) in the plane of Galactic disk derived from stars of vertical distances from the plane less than 150 pc. The solid horizontal line denotes Galactic longitude $l = 180^\circ$, and the four dashed lines denote, from bottom to top, longitudes $l = 225^\circ, 210^\circ, 150^\circ$ and 135° , respectively. An arc of 2 kpc distance is also plotted marking the approximate position of the Perseus arm.

2008). The super-bubble GSH 238+00+09 detected in the radio by Heiles (1998) is visible at a longitude of about 220° .

Berry et al. (2012) carry out a similar analysis for unresolved sources in the SDSS DR7 release based on SDSS (and 2MASS when available) photometry. Their analysis includes data collected as parts of the SEGUE, which images ten 2.5 deg wide stripes that cross the Galactic plane at selected longitudes. Some of those stripes overlap with the footprint of XSTPS-GAC. For comparison, we have cross-identified common targets analyzed by both Berry et al. (2012) and the current work. We use their results deduced with both the SDSS and 2MASS photometry available and with R_V fixed 3.0. The cross-identification is carried out using a matching radius of $1.5''$. Stars in Berry et al. (2012) with best-fit

$\chi^2 < 2$, $r < 19$ mag and $K_s < 14$ mag are selected for comparison with our results. The results are shown in Fig. 11. In spite of different set of optical photometry and reference stellar locus library adopted in the two studies, we see rather good agreement between their results and ours. Generally, the differences are well fitted by a Gaussian function (right panels of Fig. 11). With a mean and standard deviation of -0.003 ± 0.170 mag, there are no systematical differences between the two sets of determinations of extinction. For $(g - i)_0$, the scatter is a bit large for stars located on the blue portion of the stellar locus (c.f. Fig. 2), and to a less extent, for stars located near the “knee” of the stellar locus. An opposite twist is found for the extinction, although not so obvious. The twist is caused mainly by the different sets of stellar locus used and possibly in parts due to the degeneracy between the intrinsic colours and reddening. In fact, if we recalculate the best fit values of extinction A_r and intrinsic color $(g - i)_0$ using the SDSS stellar locus (Davenport et al. 2014) instead of ours, then the twist seen in the upper left panel of Fig. 11 becomes largely absent.

4.3 Two dimensional extinction maps

We construct the 2D extinction map using two methods. The first is using the best-fit A_r values from our catalog of final results. The other is to use the Rayleigh-Jeans Color Excess (RJCE) method proposed by Majewski et al. (2011) based on the 2MASS and WISE IR photometry only. We first describe the results from the RJCE method.

For the RJCE method, we use colour $(H - W2)$ to estimate extinction. In Fig. 12, we show the $(H - W2)$ v.s. $(J - K_s)$ colour-colour diagram for the high quality reference sample consisting of 132,316 stars of very low extinction (see Sect. 2). Also overplotted is an isochrone of stars of age 10 Gyr and solar metallicity $Z = 0.019$ from Girardi et al. (2002). Stars in the colour range $0.25 \leq (J - K_s) \leq 0.65$ mag, mostly main sequence dwarfs plus a few red clump giants have nearly constant $(H - W2)$ colour, with

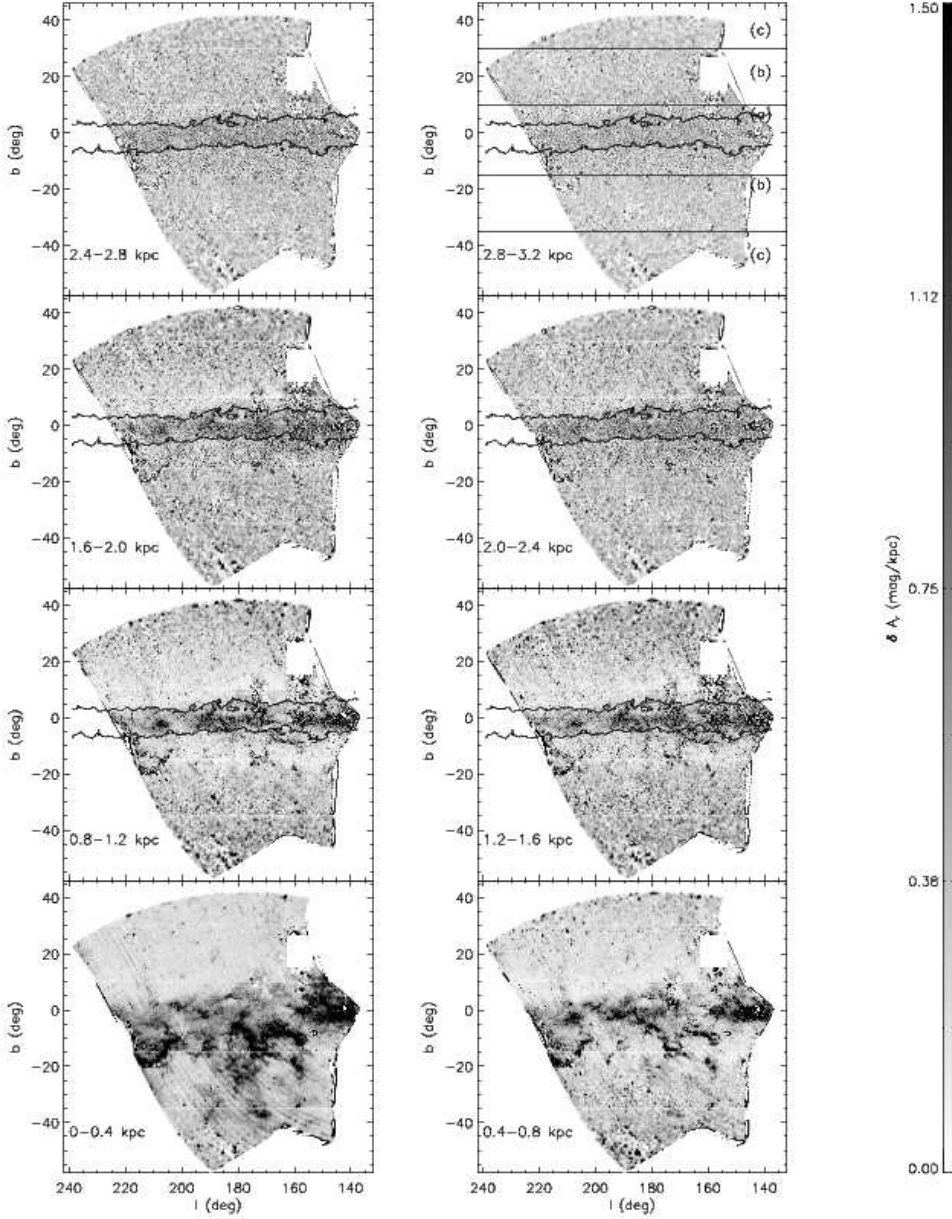


Figure 9. Extinction of individual distance bins of length 400 pc. The distance interval the extinction map refers to is marked in each panel. Different angular resolutions are adopted for regions of different Galactic latitudes, as marked in the top right panel, and are 3, 6 and 9 arcmin for regions (a), (b) and (c), respectively (see text for details). The contours overplotted in panels of large distance bins ($d > 0.8$ kpc) are integrated emission of H I gas from the LAB all-sky survey (Kalberla et al. 2005).

an average and standard deviation value of 0.083 and 0.039 mag, respectively. Accordingly, we set the zero point of $(H - W2)$ colour to $(H - W2)_0 = 0.08$ mag. Then from the extinction law of Yuan et al. (2013), we have,

$$A_r = 7.484 \times (H - W2 - 0.08) \quad (3)$$

We select stars in the 2MASS and WISE catalogs that are detected in all J , H , K_s , $W1$ and $W2$ bands and photometric errors < 0.08 mag, in the sky area, $3\text{h} < \text{R.A.} < 9\text{h}$ and $-90 < \text{Dec.} < 90$ deg, and calculate their extinction values using the above equation. The stars are then dereddened using the derived values of extinction and only stars with dereddened $(J - K_s)$ colours,

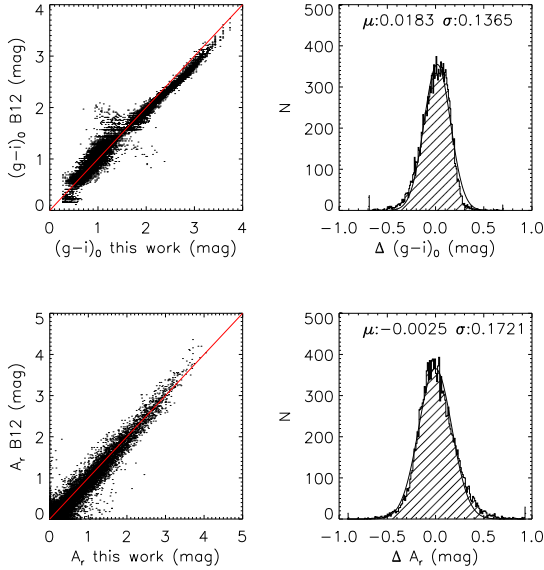


Figure 11. Comparison of best-fit values of $(g - i)_0$ (upper left panel) and A_r (lower left panel) from Berry et al. (2012) and the current work for common objects. Histograms of differences of the two sets of determinations are plotted in the right panels, for $(r - i)_0$ (top right) and A_r (bottom right), respectively.

$0.25 \leq (J - K_s)_0 \leq 0.65$ are retained. We then bin the stars into subfields, each of angular size $6' \times 6'$. A bootstrap algorithm is used to calculate the median and standard deviation (s.d.) values of extinction of all stars in a given subfield. The resultant 2D extinction map is shown in the bottom right panel of Fig. 13.

In Fig. 13 we also show the 2D extinction maps generated from our final catalog that contains best-fit values of extinction A_r . Again we bin stars in both Sample A and C separately into subfields of size $6' \times 6'$. A bootstrap algorithm is applied to calculate the median and s.d. values of extinction for stars in each subfield. Meanwhile the value of the 90th percentile of extinction and the associated s.d. of each subfield are also calculated with the same algorithm. The results are also plotted in Fig. 13. For comparison, Fig. 13 also show the SFD extinction map in the upper right panel of the diagram.

Compared to Sample C, due to the fewer number of stars available from Sample A, there are more “empty” subfields in the Sample A extinction maps than those of Sample C, in particular near the edges of footprint of the XSTPS-GAC. Also there is a notable empty patch around $l \sim 160^\circ$ and $b \sim 20^\circ$, due to abnormally large photometric errors of XSTPS-GAC fields in this area. Similar “holes” at the same location are also apparent in Fig. 9. There are also some “stripe-like” structures in the best-fit extinction maps. This is caused by the nightly varying survey depth and photometric accuracy of XSTPS-GAC. Overall, the extinction map obtained with the RJCE method agrees well with those from the best-fit SED algorithm (c.f. bottom panels of Fig. 13). Similarly, there is high degree of similarity of the overall structure and features between the best-fit 90th percentile extinction maps and that of SFD (top panels of Fig. 13). All dust features visible in the 3D maps (Fig. 9) are clearly seen in these 2D maps.

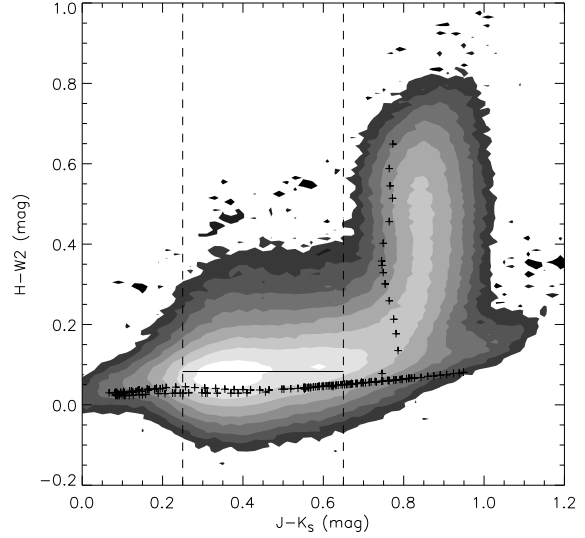


Figure 12. $(J - K_s) - (H - W2)$ colour-colour diagram for the high-quality reference sample consisting of 132,316 stars of very low extinction. Pluses delineate an isochrone of age 10 Gyr and Solar metallicity from Girardi et al. (2002). The $(J - K_s)$ colours range $[0.25, 0.65]$ is marked by two vertical dashed lines. The black horizontal line indicates a mean of 0.083 mag of $(H - W2)$ colour for stars of $(J - K_s)$ colours in the range.

To a good approximation, the 90th percentile (which exclude most of the extreme outliers) extinction maps constructed from our best-fit Samples A and C represent most of the extinction along individual lines of sight and thus can be treated as a “total” extinction map for the sky area covered. Compared to the SFD map, our “total” extinction maps show larger values for regions of high latitudes ($|b| > 15^\circ$), in particular the map from Sample C. One possible cause of this bias could be photometric errors. Another potential source of errors is the colour-reddening degeneracy, especially considering the small amount of extinction at high Galactic latitudes, typically only a factor 2–3 larger than the photometric errors (Berry et al. 2012). At low Galactic latitudes where the extinction is much larger than the photometric errors, one sees that Sample C produces the same high quantity extinction map as Sample A. At low latitudes, the SFD map yields higher extinction than ours. This may partly due to fact that the survey depth of XSTPS-GAC is not deep enough to penetrate the disk to its outer edge, in particular along sight lines of high extinction.

Fig. 14 compares values of extinction given by our Sample A median extinction to those of the previous 2D extinction maps: that of SFD in the upper panel and of Froebrich et al. (2007) in the lower panel. The SFD map gives the total extinction integrated to infinity. Therefore, for a given line of sight, the extinction yielded by the SFD map should in general be larger than our median value map. On the other hand, Arce & Goodman (1999) argue that the SFD map overestimated the extinction by 20–40% for the Taurus region. Dobashi et al. (2005) conclude that SFD overestimated the extinction value by at least a factor of two, in consistent with what found here.

Values obtained in the current work are systematically higher, by 0.2 – 0.3 mag than those obtained by Froebrich et al. (2007), who deduced their results using the near-IR colour excess (Fig. 15).

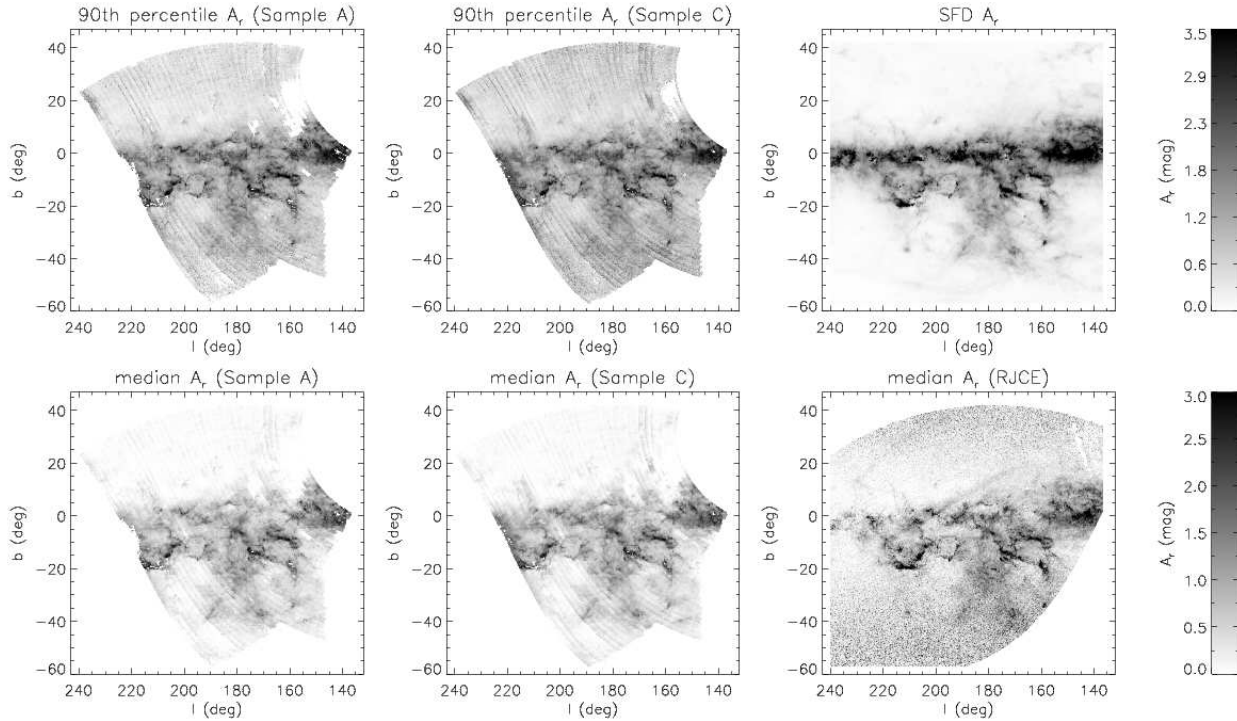


Figure 13. Two dimensional extinction maps. The top three show maps generated from the 90th percentile of extinction of Sample A (left) and C (middle), and that from SFD (right). The bottom three show maps generated from the median values of extinction of Sample A (left) and C (middle), and that generated from the median values of extinction derived using the RJCE method.

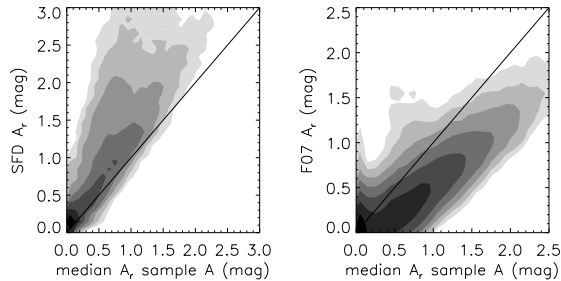


Figure 14. Values of extinction given by our Sample A median extinction map for individual sight lines are compared those predicted by the 2D maps of SFD (left) and Froebrich et al. (2007; right). In both panels, the straight line represents the curve of identity.

Note that Froebrich et al. use the extinction law of Mathis & Cardelli (1990) to convert values of $E(J - H)$ and $E(H - K_s)$ colour excess to values of visual extinction at V-band, A_V . For the Mathis & Cardelli (1990) extinction law, one has $A_V = 10.45E(J - H)$, while for that of Yuan et al. (2013) one gets $A_V = 11.92E(J - H)$. Thus applying the reddening law of Yuan et al. (2013) to the data of Froebrich et al. (2007) will reduce the systematic differences between their results and ours, but not quite enough. Another factor that may be contributing to the systematic discrepancy is that Froebrich et al. (2007) concentrate their study on dust clouds (e.g. Orion, Perseus, Taurus, Auriga, Monoceros, Camelopardalis, Cassiopeia), mostly located within 1 kpc from us (see Fig. 9). So maybe it is not surprising that their

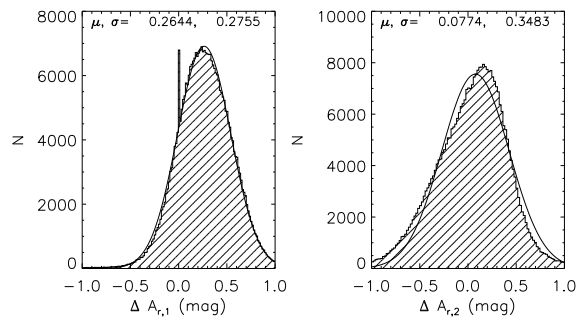


Figure 15. Left panel: Comparisons between of A_r values given by the median values of Sample A of the current work and those of Froebrich et al. (2007). Right panel: Comparison of A_r values from the integrated A_r map of Sample A of the current work, integrated to a distance of 400 pc and those of Froebrich et al., after recalibrated the latter using the extinction coefficients of Yuan et al. (2013).

reddening values are systematically lower than ours. In the right panel of Fig. 15, we compare the extinction values between A_r of Froebrich et al. (2007), after recalibrated using the extinction coefficients from Yuan et al., with those from our integrated map of distance 400 pc within which most of the dust clouds locate. Now the two sets of determinations are in good agreement, with an average difference of only 0.08 ± 0.35 mag.

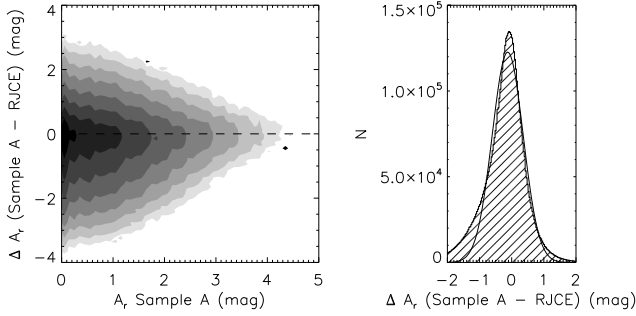


Figure 16. Difference of extinction values yielded by best-fit SED and RJCE methods plotted against extinction (left panel). A histogram of the differences is given in the right panel. The dashed line in the left panel is added to guide the eye only while the black line in the right panel is a Gaussian fit to the distribution.

5 DISCUSSION

5.1 Comparison of the RJCE and best-fit methods

Majewski et al. (2011) argue that the intrinsic ($H - W2$) colour is almost independent of spectral type and luminosity class since it measures the slope of the SED in the Rayleigh-Jeans part of the spectrum (see Fig. 2 of Majewski et al. 2011). Fig. 12 shows that the distribution of extinction free ($H - W2$) colour of dwarfs and portions of the RC stars is well represented by Gaussian distribution with a mean of 0.08 mag and a dispersion of only 0.04 mag. For red giant stars [$(J - K_s) \sim 0.8$ mag], the scatter of ($H - W2$) is much larger. The average value (i.e. zero point) of ($H - W2$) also varies. Thus in the current work, we only apply the RJCE method to stars with intrinsic ($J - K_s$) colours, $0.25 < (J - K_s)_0 < 0.65$ mag, although this RJCE method has been previously applied to giants and the RC stars by Nidever et al. (2012).

Fig. 13 shows that the extinction map obtained with the RJCE agrees with that by the best-fit SED algorithm. How do the two methods compare for individual stars? For comparison, we select stars with intrinsic colour $0.25 < (J - K_s)_0 < 0.65$ mag from Sample A and calculate their RJCE extinction using Eq. (3), and compare the results for individual stars in Fig. 16. The values of difference yielded by the two methods show a roughly Gaussian distribution with a mean close to zero but a very large dispersion of 0.5 mag. This large dispersion is found to be caused mainly by the large uncertainties for values yielded by the RJCE method. The RJCE makes use of only one colour [i.e. ($H - W2$)], while the best-fit SED algorithm employed in the current work uses seven colours. With more colours to constrain the results, the best-fit SED method obtains more robust results than the RJCE method does. This is particularly true for low extinction regions, where typical values of extinction are comparable to the photometric uncertainties. The fact that we see a dramatic increase of dispersion of values of difference for lower values of extinction (c.f. left panel of Fig. 16) demonstrate this. Note also the source confusion that WISE may be suffered from close to the Galactic plane may also affect the reliability of RJCE results significantly. Given those uncertainties, the 90th percentile extinction map deduced with the RJCE method is not shown in Fig. 13. Nevertheless, the RJCE method provides a useful approach to derive 2D extinction maps, especially when large numbers of stars of high photometric quality are available Nidever et al. (2012).

5.2 Applications of the 3D extinction maps

Comparisons with the observed colour-magnitude diagrams (CMD) serves as an important test of Galaxy stellar population synthesis models. Uttenthaler et al. (2012) and Chen et al. (2013) compare the observed CMDs between two Galactic models using 2MASS data of the Galactic Bulge. Clearly having a realistic 3D extinction map is very important for such comparisons. Both the Besançon and TRILEGAL (Girardi et al. 2005, 2012) models of the Galaxy assume a simple, linear dust opacity, $\kappa = A_V/d$, with κ typically set to a constant 0.75 mag/kpc (Lynga 1982). As we already see in reality, the extinction-distance relation is not linear at all. As an example, we have applied our 3D extinction map to Besançon and TRILEGAL simulations of a field centred on $l = 180^\circ$ and $b = 0^\circ$, and compared the results to the observed CMD from the XSTPS-GAC survey. A constant photometric error of 0.1 mag is added to photometric magnitudes simulated by the Besançon and TRILEGAL models. A limiting magnitude, $r < 18.5$ mag, is also imposed.

Fig. 17 shows that the CMDs produced by both models, reddened with extinction-distance relation from our 3D extinction map, matches well the observed CMD from the XSTPS-GAC survey. We cut the observed and model data by the completeness limits of the XSTPS-GAC survey, estimated at $r = 18.5$ mag. This completeness limit is indicated by dashed lines in Fig. 17. The CMD in the GAC region for $r < 18.5$ mag is dominated by two sequences: a sequence of dwarfs tilted towards the blue and a vertical sequence consisting mostly of the RC stars on the red. For the blue dwarf sequence, the stars become redder and redder as they go fainter and fainter (thus on average locate at larger and larger distances). We see a dramatical increase of reddening close to the limiting magnitude. We see an almost the same slope of the dwarf sequence for both the simulated and observed data, indicating the robustness of our extinction-distance relation. The simulated dwarf sequence is more diffuse and less compact compared to observed one, indicating that the 0.1 mag of photometric error added to the model is probably overestimated, particularly for bright stars. For better comparison, a more realistic model of photometric errors for the XSTPS-GAC survey data (Yuan et al. 2014, in preparation) should be used instead.

In addition to the general trend of the CMD, the star number densities on the CMD predicted by the models are at large consistent with the observations, although both models seem to predict more stars than detected by the XSTPS-GAC. Finally, we note that the TRILEGAL model predicts a prominent RC population A clump structure at $i \sim 14^m.7$ and $(g - i) \sim 2.35$ mag. The feature is however less obviously in the simulated data of Besançon as well as in the XSTPS-GAC observed data. Chen et al. (2013) notice that the Besançon model predicts too high a fraction of K giants at the Galactic center. In line with this, the current work also finds that both the TRILEGAL and Besançon models seem to predict too much giants than actually observed. These findings should help improve the models.

5.3 Comparison with CO maps

Fig. 18 compares our integrated dust extinction map as given by the 90th percentile A_v map of Sample A with that of integrated CO map from the Planck survey (Planck Collaboration et al. 2013b). The similarity of features revealed by the two maps is visually striking. The features already mentioned in Section 4, including the Orion region and the Taurus dark clouds, as well as some filamen-

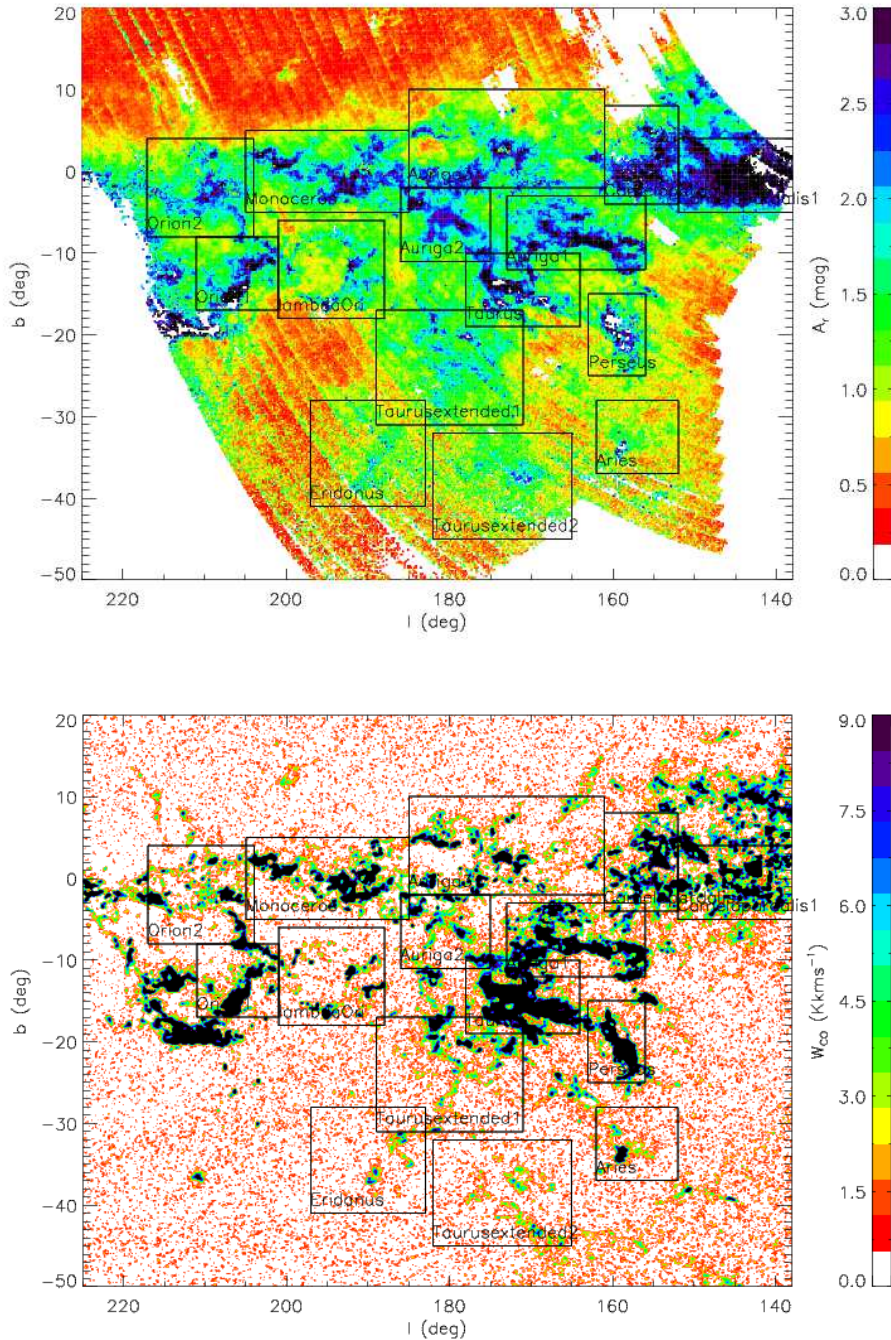


Figure 18. The distributions of the extinction (upper panel) and CO (lower panel) map in the GAC. The squares denote the dust features mentioned in the text.

tary fine features are clearly visible on both maps. Dust extinction at the optical and near-IR bands is dominated by large dust grains, while both common isotopologues of carbon monoxide, ^{12}CO and ^{13}CO , form in dusty environments, and their emission traces the gas content. The features revealed by CO gas are thinned and sharper compared to dust features. This is because that at the outer skirts of large molecular clouds where the extinction is low, the CO is likely to be largely photodissociated, producing a sharp distribution of CO emission, i.e. for regions of $A_v < 1.0$ mag, no CO emission is detected. Assuming a dust-to-gas ratio, CO is often used as

a proxy for dust extinction (e.g., Bok 1977; Frerking et al. 1982; Langer et al. 1989; Dobashi et al. 2008; Liszt 2014a,b). A recent work on the dust-to-gas ratio, the so-called X factor, is presented by Schultheis et al. (2014) for the region of Galactic center. They obtain a $X = 2.5 \times 10^{20} \text{ cm}^{-2} \text{ K}^{-1} \text{ km}^{-1} \text{ s}$, compatible to the value predicted by molecular cloud model of Glover & Mac Low (2011).

Recently, the Planck Collaboration has released CO emission maps of unprecedented quality (Planck Collaboration et al. 2013b). Those high quality CO maps, combined with the high quality dust maps obtained in the current work, should enable us to carry out a

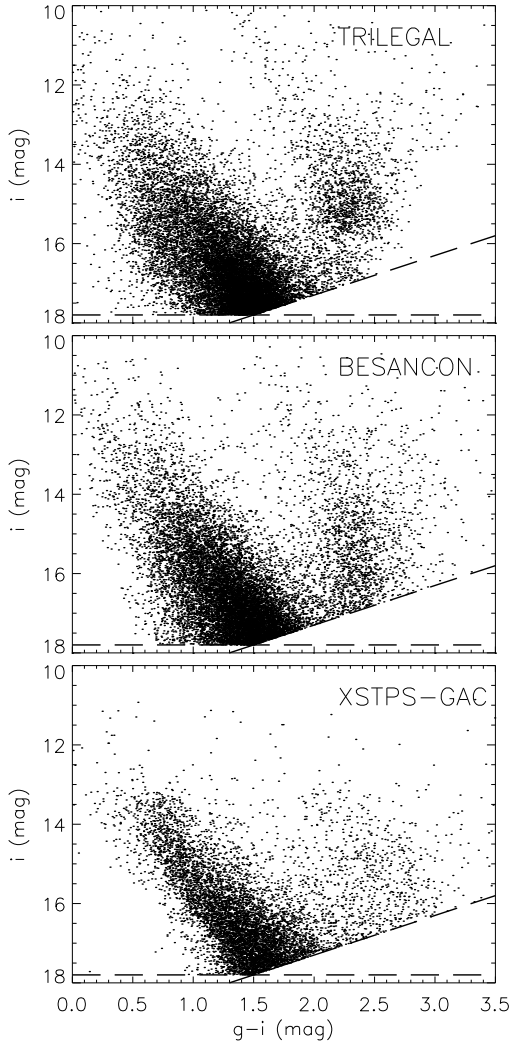


Figure 17. Colour-magnitude diagrams for field centered on $l = 180^\circ$, $b = 0^\circ$, simulated by the TRILEGAL (top panel) and Besançon (middle) models, as well as produced by the observed data from XSTPS-GAC. The simulated CMDs have been reddened using the extinction-distance relation predicted by the 3D extinction map derived in the current work. The dashed lines delineate the limiting magnitude of completeness of the XSTPS-GAC survey, estimated at $r = 18.5$ mag.

more detailed, quantitative study of the relationship between dust extinction and CO emission. Such a study will be presented in a future work.

6 CONCLUSION

By combing optical photometry from the XSTPS-GAC with those from 2MASS and WISE in the near- and mid-IR, and using a SED fitting algorithm similar to that employed by Berry et al.

(2012), we have constructed the first comprehensive quality 3D extinction map for a large sky area centered on the GAC. The map covers $6,000 \text{ deg}^2$ at angular resolutions between $3 - 9$ arcmin, out to a distance of 4 kpc. The extinction map is available online at CDS as well as at a website hosted at the Peking University (<http://162.105.156.243/site/Photometric-Extinctions-and-Distances/>). Compared to 2D SFD map, our 3D map should produce better results for disk stars of low latitudes, where the SFD map may have overestimated the extinction by a factor of 2–3. A RJCE method is also used to generate a 2D extinction map, yielding results compatible with those deduced from the best-fit SED algorithm. However for individual stars, the RJCE method tends to yield results of larger uncertainty. We show that by combining large multi-band surveys, such as the XSTPS-GAC, 2MASS and WISE, one is able to constrain the interstellar extinction for individual stars. The combination of optical and IR data can break the degeneracy between the effective temperature T_{eff} [or equivalently the intrinsic colour $(g - i)_0$] and the extinction A_r . By making use of more photometric bands that range from the optical to the IR, the SED fitting method yields results that are generally more robust than the RJCE/NICE(R) method does, which is based on two IR bands only.

In this process, we have also constructed a reference catalog consisting of 132,316 stars of essentially zero extinction with quality photometry from the XSTPS-GAC for optical bands and from the 2MASS and WISE for IR bands. The reference catalog is used to construct standard stellar locus employed by the SED fitting algorithm. Both the reference catalog and the standard stellar locus are available online from the aforementioned websites.

The 3D extinction map presented in the current work should be quite useful for follow-up analyse of LSS-GAC data, as well as data from other surveys.

ACKNOWLEDGEMENTS

We want to thank the referee for detailed and constructive comments that help improve the manuscript significantly. This work is partially supported by National Key Basic Research Program of China 2014CB845700 and National Natural Science Foundation of China grant #11078006.

This work has made use of data products from the Guoshoujing Telescope (the Large Sky Area Multi-Object Fibre Spectroscopic Telescope, LAMOST). LAMOST is a National Major Scientific Project built by the Chinese Academy of Sciences. Funding for the project has been provided by the National Development and Reform Commission. LAMOST is operated and managed by the National Astronomical Observatories, Chinese Academy of Sciences.

This publication makes use of data products from the Two Micron All Sky Survey, which is a joint project of the University of Massachusetts and the Infrared Processing and Analysis Center/California Institute of Technology, funded by the National Aeronautics and Space Administration and the National Science Foundation.

This publication makes use of data products from the Wide-field Infrared Survey Explorer, which is a joint project of the University of California, Los Angeles, and the Jet Propulsion Laboratory/California Institute of Technology, funded by the National Aeronautics and Space Administration.

REFERENCES

- An, D., et al. 2008, *ApJS*, 179, 326
- Arce, H. G. & Goodman, A. A. 1999, *ApJ*, 512, L135
- Arenou, F., Grenon, M., & Gomez, A. 1992, *A&A*, 258, 104
- Bailer-Jones, C. A. L. 2011, *MNRAS*, 411, 435
- Bajaja, E., Arnal, E. M., Larrarte, J. J., Morras, R., Pöppel, W. G. L., & Kalberla, P. M. W. 2005, *A&A*, 440, 767
- Benjamin, R. A., et al. 2005, *ApJ*, 630, L149
- Berry, M., et al. 2012, *ApJ*, 757, 166
- Boggess, N. W., et al. 1992, *ApJ*, 397, 420
- Bok, B. J. 1977, *PASP*, 89, 597
- Bond, N. A., et al. 2010, *ApJ*, 716, 1
- Burstein, D. & Heiles, C. 1982, *AJ*, 87, 1165
- Cardelli, J. A., Clayton, G. C., & Mathis, J. S. 1989, *ApJ*, 345, 245
- Chen, B., Figueras, F., Torra, J., Jordi, C., Luri, X., & Galadí-Enríquez, D. 1999, *A&A*, 352, 459
- Chen, B., Vergely, J. L., Valette, B., & Carraro, G. 1998, *A&A*, 336, 137
- Chen, B. Q., Schultheis, M., Jiang, B. W., Gonzalez, O. A., Robin, A. C., Rejkuba, M., & Minniti, D. 2013, *A&A*, 550, A42
- Covey, K. R., et al. 2007, *AJ*, 134, 2398
- Dame, T. M., Hartmann, D., & Thaddeus, P. 2001, *ApJ*, 547, 792
- Davenport, J. R. A., et al. 2014, *ArXiv e-prints*
- Dobashi, K., Bernard, J.-P., Hughes, A., Paradis, D., Reach, W. T., & Kawamura, A. 2008, *A&A*, 484, 205
- Dobashi, K., Uehara, H., Kandori, R., Sakurai, T., Kaiden, M., Umemoto, T., & Sato, F. 2005, *PASJ*, 57, 1
- Drimmel, R., Cabrera-Lavers, A., & López-Corredoira, M. 2003, *A&A*, 409, 205
- Eisenstein, D. J., et al. 2006, *ApJS*, 167, 40
- Finlator, K., et al. 2000, *AJ*, 120, 2615
- Fitzpatrick, E. L. 1999, *PASP*, 111, 63
- Fitzpatrick, E. L. & Massa, D. 2009, *ApJ*, 699, 1209
- Flaherty, K. M., Pipher, J. L., Megeath, S. T., Winston, E. M., Gutermuth, R. A., Muzerolle, J., Allen, L. E., & Fazio, G. G. 2007, *ApJ*, 663, 1069
- Frerking, M. A., Langer, W. D., & Wilson, R. W. 1982, *ApJ*, 262, 590
- Froebrich, D., Murphy, G. C., Smith, M. D., Walsh, J., & Del Burgo, C. 2007, *MNRAS*, 378, 1447
- Gao, J., Jiang, B. W., & Li, A. 2009, *ApJ*, 707, 89
- Geller, A. M., Mathieu, R. D., Braden, E. K., Meibom, S., Platais, I., & Dolan, C. J. 2010, *AJ*, 139, 1383
- Girardi, L., et al. 2012, *TRILEGAL*, a TRIdimensional modeL of the GALaxy: Status and Future, ed. A. Miglio, J. Montalbán, & A. Noels, 165
- Girardi, L., Bertelli, G., Bressan, A., Chiosi, C., Groenewegen, M. A. T., Marigo, P., Salasnich, B., & Weiss, A. 2002, *A&A*, 391, 195
- Girardi, L., Groenewegen, M. A. T., Hatziminaoglou, E., & da Costa, L. 2005, *A&A*, 436, 895
- Glover, S. C. O. & Mac Low, M.-M. 2011, *MNRAS*, 412, 337
- Gonzalez, O. A., Rejkuba, M., Zoccali, M., Valenti, E., Minniti, D., Schultheis, M., Tobar, R., & Chen, B. 2012, *A&A*, 543, A13
- Green, G. M., et al. 2014, *ApJ*, 783, 114
- Hanson, R. J. & Bailer-Jones, C. A. L. 2014, *MNRAS*, 438, 2938
- Hawley, S. L., et al. 2002, *AJ*, 123, 3409
- Heiles, C. 1998, *ApJ*, 498, 689
- High, F. W., Stubbs, C. W., Rest, A., Stalder, B., & Challis, P. 2009, *AJ*, 138, 110
- Indebetouw, R., et al. 2005, *ApJ*, 619, 931
- Ivezić, Ž., et al. 2008, *ApJ*, 684, 287
- Ivezić, Ž., et al. 2007, *AJ*, 134, 973
- Jiang, B. W., Gao, J., Omont, A., Schuller, F., & Simon, G. 2006, *A&A*, 446, 551
- Jones, D. O., West, A. A., & Foster, J. B. 2011, *AJ*, 142, 44
- Jurić, M., et al. 2008, *ApJ*, 673, 864
- Kalberla, P. M. W., Burton, W. B., Hartmann, D., Arnal, E. M., Bajaja, E., Morras, R., & Pöppel, W. G. L. 2005, *A&A*, 440, 775
- Kalirai, J. S., Fahlman, G. G., Richer, H. B., & Ventura, P. 2003, *AJ*, 126, 1402
- Lallement, R., Vergely, J.-L., Valette, B., Puspitarini, L., Eyer, L., & Casagrande, L. 2014, *A&A*, 561, A91
- Langer, W. D., Wilson, R. W., Goldsmith, P. F., & Beichman, C. A. 1989, *ApJ*, 337, 355
- Lejeune, T., Cuisinier, F., & Buser, R. 1997, *A&AS*, 125, 229
- Lejeune, T., Cuisinier, F., & Buser, R. 1998, *A&AS*, 130, 65
- Liszt, H. 2014a, *ApJ*, 783, 17
- Liszt, H. 2014b, *ApJ*, 780, 10
- Liu, X.-W., et al. 2014, in Feltzing S., Zhao G., Walton N., White-lock P., eds, *Proc. IAU Symp. 298, Setting the scene for Gaia and LAMOST*, Cambridge University Press, pp. 310-321, preprint (arXiv: 1306.5376)
- Lombardi, M. & Alves, J. 2001, *A&A*, 377, 1023
- Lombardi, M., Alves, J., & Lada, C. J. 2011, *A&A*, 535, A16
- Lynga, G. 1982, *A&A*, 109, 213
- Majewski, S. R., Zasowski, G., & Nidever, D. L. 2011, *ApJ*, 739, 25
- Marshall, D. J., Joncas, G., & Jones, A. P. 2009, *ApJ*, 706, 727
- Marshall, D. J., Robin, A. C., Reylé, C., Schultheis, M., & Picaud, S. 2006, *A&A*, 453, 635
- Martin, D. C., et al. 2005, *ApJ*, 619, L1
- Mathis, J. S. & Cardelli, J. A. 1990, in *Bulletin of the American Astronomical Society*, Vol. 22, *Bulletin of the American Astronomical Society*, 861
- Meisner, A. M. & Finkbeiner, D. P. 2014, *ApJ*, 781, 5
- Morrison, J. E., McLean, B., & GSC-Catalog II Construction Team. 2001, in *Bulletin of the American Astronomical Society*, Vol. 33, *AAS/Division of Dynamical Astronomy Meeting #32*, 1194
- Neckel, T., Klare, G., & Sarcander, M. 1980, *A&AS*, 42, 251
- Neugebauer, G., et al. 1984, *ApJ*, 278, L1
- Nidever, D. L., Zasowski, G., & Majewski, S. R. 2012, *ApJS*, 201, 35
- Nishiyama, S., Tamura, M., Hatano, H., Kato, D., Tanabé, T., Sugitani, K., & Nagata, T. 2009, *ApJ*, 696, 1407
- O'Donnell, J. E. 1994, *ApJ*, 422, 158
- Peek, J. E. G. & Graves, G. J. 2010, *ApJ*, 719, 415
- Planck Collaboration, et al. 2013a, *ArXiv e-prints*
- Planck Collaboration, et al. 2013b, *ArXiv e-prints*
- Randich, S., Sestito, P., Primas, F., Pallavicini, R., & Pasquini, L. 2006, *A&A*, 450, 557
- Richards, G. T., et al. 2001, *AJ*, 121, 2308
- Robin, A. C., Marshall, D. J., Schultheis, M., & Reylé, C. 2012, *A&A*, 538, A106
- Robin, A. C., Reylé, C., Derrière, S., & Picaud, S. 2003, *A&A*, 409, 523
- Rowles, J. & Froebrich, D. 2009, *MNRAS*, 395, 1640
- Sale, S. E. 2012, *MNRAS*, 427, 2119
- Sale, S. E., et al. 2009, *MNRAS*, 392, 497
- Schlafly, E. F. & Finkbeiner, D. P. 2011, *ApJ*, 737, 103
- Schlafly, E. F., Finkbeiner, D. P., Schlegel, D. J., Jurić, M., Ivezić,

- Ž., Gibson, R. R., Knapp, G. R., & Weaver, B. A. 2010, *ApJ*, 725, 1175
- Schlafly, E. F., et al. 2014, *ApJ*, 786, 29
- Schlegel, D. J., Finkbeiner, D. P., & Davis, M. 1998, *ApJ*, 500, 525
- Schultheis, M., et al. 2014, ArXiv e-prints
- Schultheis, M., et al. 1999, *A&A*, 349, L69
- Skrutskie, M. F., et al. 1997, in *Astrophysics and Space Science Library*, Vol. 210, *The Impact of Large Scale Near-IR Sky Surveys*, ed. F. Garzon, N. Epchtein, A. Omont, B. Burton, & P. Persi, 25
- Smolčić, V., et al. 2004, *ApJ*, 615, L141
- Straizys, V. & Laugalys, V. 2008, *Baltic Astronomy*, 17, 1
- Straizys, V., Cernis, K., Kazlauskas, A., & Meistas, E. 1992, *Baltic Astronomy*, 1, 149
- Taylor, B. J., Joner, M. D., & Jeffery, E. J. 2008, *ApJS*, 176, 262
- Uttenthaler, S., Schultheis, M., Nataf, D. M., Robin, A. C., Lebzelter, T., & Chen, B. 2012, *A&A*, 546, A57
- Wright, E. L., et al. 2010, *AJ*, 140, 1868
- Wu, Z.-Y., Zhou, X., Ma, J., & Du, C.-H. 2009, *MNRAS*, 399, 2146
- Xin, Y. & Deng, L. 2005, *ApJ*, 619, 824
- Yadav, R. K. S., et al. 2008, *A&A*, 484, 609
- Yanny, B., et al. 2009, *AJ*, 137, 4377
- York, D. G., et al. 2000, *AJ*, 120, 1579
- Yuan, H. B., Liu, X. W., & Xiang, M. S. 2013, *MNRAS*, 430, 2188
- Yuan, H.-B., Liu, X.-W., Xiang, M.-S., Huo, Z.-Y., Zhang, H.-H., Huang, Y., & Zhang, H.-W. 2014, in *Feltzing S., Zhao G., Walton N., Whitelock P., eds. Proc. IAU Symp. 298, Setting the scene for Gaia and LAMOST*, Cambridge University Press, pp. 240-245, preprint (arXiv: 1306.5614)
- Zhang, H.-H., Liu, X.-W., Yuan, H.-B., Zhao, H.-B., Yao, J.-S., Zhang, H.-W., & Xiang, M.-S. 2013, *Research in Astronomy and Astrophysics*, 13, 490
- Zhang, H.-H., Liu, X.-W., Yuan, H.-B., Zhao, H.-B., Yao, J.-S., Zhang, H.-W. Xiang, M.-S., & Huang, Y. 2014, *Research in Astronomy and Astrophysics*, 14, 456